

THE LYMAN ALPHA FOREST FROM GRAVITATIONAL COLLAPSE IN THE CDM+ Λ MODEL

Jordi Miralda-Escudé ¹, Renyue Cen ², Jeremiah P. Ostriker ² and Michael Rauch ^{3, 4}

Email: jordi@sns.ias.edu, cen@astro.princeton.edu,
jpo@astro.princeton.edu, mr@astro.caltech.edu

Received: 1995,

ABSTRACT

We use an Eulerian hydrodynamic cosmological simulation to model the Ly α forest in a spatially flat, COBE normalized, cold dark matter model with $\Omega = 0.4$, and find that the intergalactic, photoionized gas is predicted to collapse into sheet-like and filamentary structures which give rise to absorption lines having similar characteristics as the observed Ly α forest. A typical filament is $\sim 1h^{-1}$ Mpc long with thickness $\sim 50 - 100h^{-1}$ kpc (in proper units), and baryonic mass $\sim 10^{10}h^{-1} M_{\odot}$. In comparison our nominal numerical resolution is $(2.5, 9)h^{-1}$ kpc (in the two simulations we perform) with true resolution, perhaps a factor of 2.5 worse than this; the nominal mass resolution is $(10^{4.2}, 10^{5.8})M_{\odot}$ in gas for the two simulations. The gas temperature increases with time as structures with larger velocities collapse gravitationally.

We show that the predicted distributions of column densities, b-parameters and equivalent widths of the Ly α forest clouds agree with the observed ones, and that their evolution is consistent with our model, if the ionizing background has (as expected from our simulations) an approximately constant intensity between $z = 2$ and $z = 4$. The new method of identifying lines as contiguous regions in the spectrum below a fixed flux threshold is suggested to analyze the absorption lines, given that the Ly α spectra arise from a continuous density field of neutral hydrogen rather than discrete clouds. We also predict the distribution of transmitted flux and its correlation along a spectrum and on parallel spectra, and the He II flux decrement as a function of redshift. We predict a correlation length of $\sim 80h^{-1}$ kpc perpendicular to the line of sight for features in the Lyman alpha forest.

¹ Institute for Advanced Study, Princeton, NJ 08540

² Peyton Hall, Princeton University, Princeton, NJ 08544

³, California Institute of Technology, Pasadena, CA 91125

⁴ Hubble Fellow

In order to reproduce the observed number of lines and average flux transmission, the baryon content of the clouds may need to be significantly higher than in previous models because of the low densities and large volume-filling factors we predict. If the background intensity $J_{H\,I}$ is at least that predicted from the observed quasars, Ω_b needs to be as high as $\sim 0.025h^{-2}$, higher than expected by light element nucleosynthesis; the model also predicts that most of the baryons at $z > 2$ are in Ly α clouds, and that the rate at which the baryons move to more overdense regions is slow. A large fraction of the baryons which are not observed at present in galaxies might be intergalactic gas in the currently collapsing structures, with $T \sim 10^5 - 10^6$ K.

Subject headings: intergalactic medium - quasars: absorption lines - cosmology: large-scale structure of Universe - hydrodynamics

1. INTRODUCTION

Most of the information available to us by direct observation of epochs far removed from the present is in the increasingly detailed absorption spectra of high redshift quasars. The very numerous lines in the Lyman alpha forest are believed to arise primarily from neutral hydrogen along the line of sight, enabling us to study the distribution of neutral gas over a wide redshift range (from the present to the highest redshift quasars). By now we can typically observe hundreds of lines per unit redshift along each line of sight, with each line yielding an HI column density N_{HI} , a Doppler width b , and a redshift z . Thus, large samples of absorption lines can be obtained by observing only a relatively small number of quasars. By now fairly good data is available characterizing the distribution of b and N_{HI} as a function of redshift, and the correlations of the lines (e.g., Carswell et al. 1991; Rauch et al. 1993; Petitjean et al. 1993; Schneider et al. 1993; Cristiani et al. 1995; Hu et al. 1995; Tytler et al. 1995). In addition, as we shall discuss in this paper, the fluctuations in the transmitted flux which cannot be separated into individual lines also contain a large amount of information. The Ly α absorption lines also provide a “fair” sample, in the sense that the lines of sight to distant quasars pass through random parts of the intervening universe. Thus the usual issues of selection and bias are not as serious here as when studying other cosmic phenomena.

Until quite recently there was very little attempt to use this large data base to constrain theories for the origin of structure. Theories of the Ly α forest were attempts at heuristic modeling rather than *ab initio* theories. One aimed to make a local model for the gas responsible for the absorption, with sufficient physical detail to understand the degree of ionization of the gas, its temperature and density, the processes responsible for confinement in clumps (i.e., the fact that individual lines are seen), and finally to account for the observed statistical properties. Some of these models were based on the hypothesis of a hot intergalactic medium created by early shock heating, which could cool into clouds that would be confined by the hot gas (Sargent et al. 1980; Ostriker & Ikeuchi 1983; Ikeuchi & Ostriker 1986). Clouds associated with galaxies were another dominant idea. Bahcall & Spitzer (1969) suggested that galaxies were surrounded by halos of hot gas, which could contain some photoionized clouds in pressure equilibrium. Another early paper by Arons (1972) proposed that the clouds could be associated with infalling gas around forming galaxies. Other recent suggestions include the possible association of Ly α clouds with the outer parts of HI disks (Charlton, Salpeter, & Hogan 1993), the debris from merging satellites (Wang 1993; Morris & van den Bergh 1994), galactic outflows (Fransson & Epstein 1982, Wang 1995) or primordial, linear density fluctuations in the intergalactic medium (Bi 1993). Rees (1986) and Ikeuchi (1986) suggested that the clouds were related to subgalactic “minihalos” where the photoionized gas could be maintained in thermal and dynamical equilibrium. A more detailed study was presented in the classic paper by Bond, Szalay, & Silk (1988), where hydrodynamic simulations of spherical halos were made which suggested that the absorption lines could arise in gas around the dark matter halos predicted by the cold dark matter model. This gas could either be infalling and contracting if the halo was sufficiently massive, or expanding after having been reheated during reionization. The level of semianalytic modeling possible at the time this seminal paper was written did not allow for accurate predictions to be made, which could tell whether or not the proposed theory was correct. Now, with the advances of computational capabilities, one can directly model the three dimensional growth of small scale structure of any *ab initio* model and then shoot lines of sight through the simulation to collect mock observational spectra which can be compared with real data.

At this point, we wish to remark that the models for the formation of structure in the universe from primordial fluctuations represent an unprecedented step in the history of science. Up to now, the physical laws of nature have only attempted to explain or predict the evolution of a physical system once a set of initial conditions have been determined observationally, which can fix the state of the system at an initial time. The models for the origin of structure specify the statistical ensemble of the initial conditions for the universe, and they should in principle fully predict the subsequent evolution of the universe and the observations we can make, without the need of other observations to fix any initial conditions. It is only our inability to calculate complex physical phenomena such as cloud formation from cooled gas, star formation, supernova explosions, dust formation, etc. which prevents us from fully realising the predictive potential of the models and testing them against observations. At present, we still do not know which model of structure formation should be correct, and there is also a number of constants which are free parameters in the models (such as the baryon to dark matter ratio, the specific entropy of the universe, and the amplitude of the density fluctuations) and must be determined by observation. It is hoped that a more complete theory in the future will also predict these quantities.

In order to test such models, we need to identify certain objects and physical phenomena taking place in the universe which are sufficiently simple to allow us to predict what should be observed. The observations that can be most reliably predicted are those of the fluctuations in the microwave background, since these fluctuations were produced when all the structures were still in the linear regime (although they are superposed with other fluctuations arising after non-linear collapse, such as the Sunyaev-Zeldovich effect). However, most of our observations of the universe are of objects that have long been in the non-linear regime at later epochs. The distribution and abundances of galaxies and X-ray clusters have long been used as a test of the models of structure formation, since these are the objects most easily observed near us. At high redshift, galaxies and clusters become progressively faint, whereas the Ly α forest offers us an excellent probe to directly observe the evolution of the neutral hydrogen distribution.

In addition to the observational advantages, the Ly α forest may also have the advantage of allowing fairly precise theoretical predictions of its observable properties. The Ly α absorption spectra allow us to observe gas at lower densities than any other observational method. In fact, the most underdense gas in the voids should, as we shall show in this paper, cause fluctuations in the optical depth between Ly α lines that are observable, and all the neutral gas at intermediate densities, up to the dense central regions in halos where galaxies should form, is also observable as absorption lines of increasing column density with increasing gas density. This gives an enormous advantage over the study of galaxies, which are indicating the regions where the gas densities became high enough for star formation to take place, or over X-ray observations, which are sensitive to objects having high X-ray surface brightness, corresponding to dense gas in the virialized regions of galaxy clusters. The processes affecting the low density gas may be sufficiently simple as to allow detailed modeling and predictability, and therefore provide powerful tests for the models of the origin of structure. This is not possible at high densities, where the gas will typically develop a complicated structure (such as in the interstellar medium of our galaxy), and star formation will be taking place.

The low density gas is affected by gravitational and pressure forces, which are predicted in detail. In addition, the gas temperature is influenced by the ionizing radiation, which is responsible for the heating after reionization and for providing a natural scale, the Jeans scale, for the smallest objects

where the photoionized gas will collapse. It is this process of reheating that allows us to calculate the gas distribution with the finite resolution of our numerical code, even when the smallest structures in the dark matter are unresolved. However, the presence of the ionizing background introduces two sources of uncertainty: first, during the epoch of reionization the intergalactic medium becomes highly inhomogeneous as sources of ionizing photons start to emit, with individual H II regions expanding from the sources and patches of neutral gas left in between (Arons & Wingert 1972). After reionization is complete, the photoionized gas is left at a temperature that depends on the spectrum of the emitted radiation, and which could spatially fluctuate depending on the epoch at which each region was reionized (Miralda-Escudé & Rees 1994). Second, once all the gas is ionized, the discrete number of sources combined with a large number of absorbers can cause fluctuations in the intensity of the ionizing background (Zuo 1992a,b; Fardal & Shull 1993), and correspondingly change the neutral gas density. Inasmuch as the process of formation of the sources of radiation (presumably quasars and young stellar populations in galaxies) is not currently understood, such effects cannot be predicted, but they can only be calibrated from observations. In this paper, we shall assume a uniform radiation background at all epochs, ignoring the effects mentioned above (these are not likely to be very large, because the expected fluctuations in intensity and temperature should be small except at very high redshift).

In addition to the uncertainties related to the ionizing background, there is also the possibility that kinetic energy is released to the intergalactic medium from explosions in the gravitationally collapsed objects (probably arising from active galactic nuclei or supernova explosions in starbursts). Other work which we have done (Cen & Ostriker 1993a) indicates that such explosive input can alter the properties of the gas considerably in the vicinity of virialized objects, but is relatively unimportant in the bulk of the cosmic volume in which most of the QSO absorption features are found. Thus, in this work we do not include any energetic input from the collapsed regions; we hope to investigate the effects of explosions in due course.

To summarize, the input to our simulations is, in addition to the model for the initial density fluctuations and the cosmological parameters adopted, the background radiation field which we evolve explicitly in time, assuming it is spatially uniform at all times, and the specific numerical scheme for solving the hydrodynamic equations and its implementation. Initial results of this work were presented in Cen et al. (1994; hereafter Paper I); we use an Eulerian hydrodynamic code and treat a low density, spatially flat cold dark matter (CDM) model. More recently, a similar approach has been followed by Zhang et al. (1995) who use a similar Eulerian code and examine a more standard $\Omega = 1$ COBE-normalized CDM scenario, and by Hernquist et al. (1995, hereafter HKWM), who use an SPH (particle based) hydro code and the same CDM model with a lower normalization, more appropriate to reproduce the observed abundance of clusters (see also Petitjean et al. 1995, who again take a similar approach but without using a hydro code). All of these groups, despite the differences in technical approach and adopted model found surprisingly good agreement between the simulated and real Ly α forest. Differences among the simulations and with the observations will probably appear as the results are scrutinized in more detail; however, the overall agreement (which is reinforced by the results in this paper) makes it quite probable that the physical environment produced by the codes of widely distributed photoionized gas in sheets and filaments associated with caustics, outside of virialized objects, does correspond to the real world.

In this paper, we return to the simulations of Paper I to provide greater detail concerning our

physical modeling and, more importantly, to present a much more detailed analysis of our (mock) observations. The results of Paper I were based on simulations on a box of $3h^{-1}$ Mpc; here, we shall include results from a larger simulation in a box of $10h^{-1}$ Mpc, comparing the results to see the effects of the large-scale power.

Before beginning the detailed discussion of our results, it may be useful to say a few words of comparison of the two detailed hydrodynamic methods mentioned earlier. Roughly speaking, the Eulerian technique, in its current application, has advantages with regard to mass resolution and the SPH technique with regard to spatial resolution. The average gas mass per cell in our large box simulation (with a length of $10h^{-1}$ Mpc and 288^3 cells) is $6 \times 10^5 M_\odot$, and the cell size is $35h^{-1}$ kpc in comoving units; if we take the actual spatial resolution to be 2.5 cells, this gives $90h^{-1}$ kpc. In the SPH simulation of HKWM (with a box of length $11.1 h^{-1}$ Mpc) the mass per gas particle was $1.5 \times 10^8 M_\odot$, and the maximal spatial resolution was $10h^{-1}$ comoving kpc (equivalent to $6.5h^{-1}$ kpc Plummer softening). Thus that method was able to identify and determine the properties of the rare, very high density features which correspond to the damped Ly α and Lyman limit systems (Katz et al. 1995), which could not be treated with the Eulerian codes. However, HKWM note (and we concur) that the typical Ly α cloud arises from material having rather modest overdensity in the range $\rho/\bar{\rho} = 1 - 10$. If the fluid is overdense by a factor of 10, the sphere containing 20 particles (roughly the number required to define local properties in an SPH code) has a diameter of $270 h^{-1}$ kpc in the HKWM simulation. Thus, for the bulk of the small clouds in regions of modest overdensity the Eulerian code has both greater mass and greater spatial resolution. But, to be quantitative on the advantages of the particle codes, at an overdensity $\gtrsim 300$ (appropriate for the high column density systems) the spatial resolution of the SPH code exceeds that attainable by the Eulerian code.

After describing several aspects of the simulations in §2, we present the physical characteristics of the absorbing structures in §3. The analysis of the simulated spectra is given in §4; detailed predictions of our model are given there for the distribution and correlation properties of the transmitted flux, and properties of the absorption lines and their correlations along a single line of sight and on parallel lines of sight. In §5 we discuss some aspects of the Ly α forest that are derived from our model, especially the fraction of baryons that is contained in absorption systems of different column densities. Finally, our conclusions are summarized in §6.

2. THE SIMULATION

We use the same Eulerian code that was used for the simulations in Paper I. As will be shown below, many Ly α lines originate from regions enclosed by two semi-planar shocks propagating outwards. It is therefore essential to model these shocks accurately. We use a new shock-capturing cosmological hydrodynamic code based on Harten's Total Variation Diminishing (TVD) hydrodynamic scheme (Harten 1984), described in Ryu et al. (1993). The original TVD scheme was improved by adding one additional variable (entropy) and its evolution equation to the conventional hydrodynamic equations. This improvement allows us to eliminate otherwise large artificial entropy generation in regions where the gas is not shocked. In fact, typical, unphysical high temperatures being generated due to inaccuracy in the conventional hydrodynamic code are around $10^4 - 10^5$ K

when the true temperatures would be much lower. This affects the formation of Ly α clouds most severely; thus, this modification was absolutely necessary to use the code for the problem of Ly α clouds. Details on this subtle treatment can be found in Ryu et al. (1993).

We adopt the same model as in Paper I, a CDM+ Λ model with $\Omega = 0.4$, $\Omega_b = 0.0355$ (cf. Walker et al. 1991), $\lambda = 0.6$, $h = 0.65$ and $\sigma_8 = 0.79$ (first-year COBE normalization; Efstathiou, Bond, & White 1992; Kofman, Gnedin, & Bahcall 1993). The second-year COBE data gives a σ_8 about 15% higher; Stompor & Gorski 1994; White & Bunn 1995) but a very small tilt ($n < 1$) in the spectrum would recover the initial conditions that we take (for scales $L \leq 10h^{-1}\text{Mpc}$) while retaining the CBR normalization (cf. Ostriker & Steinhardt 1995). In Paper I, we presented preliminary results from two simulations on a box of size $3h^{-1}\text{Mpc}$: the first one with $N = 288^3$ cells and 144^3 dark matter particles, which we shall denote as the L3 simulation in this paper, and the second one with 144^3 cells and 72^3 dark matter particles, which will be denoted as the l3 simulation. This paper will examine much more thoroughly a simulation on a box of $10h^{-1}\text{Mpc}$ with 288^3 cells, which we call the L10 simulation, and we shall compare the results to the L3 and l3 simulations on the smaller box. As we shall see, the effects of the large-scale power that can be included in the L10 simulation are substantially important, whereas the differences between the L3 and l3 simulations are small suggesting that the resolution employed is sufficient for reproducing the Ly α clouds. The cell size in the L10 simulation is $35h^{-1}\text{kpc}$ (comoving) corresponding to a baryonic mass of $6.3 \times 10^5 M_\odot$. The power spectrum transfer function is computed using the method described in Cen, Gnedin, & Ostriker (1993).

Atomic processes within a primeval plasma of hydrogen and helium of composition (76%, 24%) in mass are all included using the same heating, cooling, and ionization terms as in Cen (1992). We calculate self-consistently the average background photoionizing radiation field as a function of frequency, assuming the radiation field is uniform. The evolution of the radiation field is calculated given the average attenuation in the simulated box and the emission (both from the gas itself and from the assumed sources of ionizing photons). The time-dependent equations for the ionization structure of the gas are solved by iteration using an implicit method, to avoid the instabilities that arise in solving stiff equations. In general, the abundances of different species are close to ionization equilibrium after most of the gas has been photoionized, when the universe becomes optically thin and the intensity of the ionizing background starts rising. However, before reionization is complete the intensity of ionizing photons is very low and the ionization timescale correspondingly long, so ionization equilibrium cannot be assumed.

At every timestep during the simulation, two-dimensional tables as a function of density and pressure of the gas are made giving the rates of ionization and recombination for each species, as well as the cooling and heating rate and the radiation emissivity rate, given the spectrum of the background radiation at that timestep. Interpolation within this table is then used to calculate these quantities at every cell, allowing us to speed up the calculation by a large factor and to solve for the ionization of the gas using the time-dependent equations. This approach is an improvement over the assumption of ionization equilibrium; in particular, it is absolutely necessary to use as the gas is being reionized. In this way, we ensure that the energy of reionization (i.e., the average thermal energy given by the photoionization of every hydrogen atom) is correctly deposited on the gas. The assumption of ionization equilibrium would lead to a very low initial temperature for the intergalactic gas, because the gas is suddenly ionized as the intensity of the background rises, and

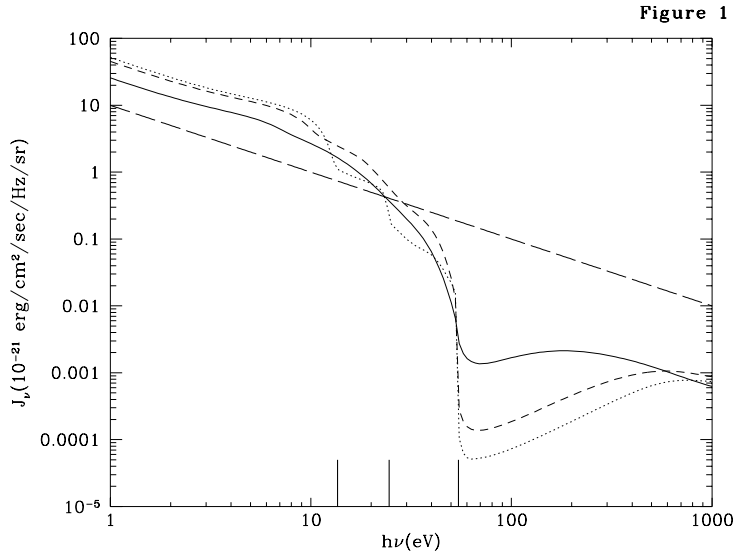


Figure 1: The radiation field in the simulation is shown for three different redshifts $z=2$ (solid curve), $z=3$ (dashed curve) and $z=4$ (dotted curve). Also shown for comparison as a long dashed line is a power-law case with index -1 (used in HKWM); our radiation spectra are softer due in part to our intrinsic spectra and to the absorption effects.

it is then heated only at the rate at which the ions can recombine and be photoionized again. It needs to be pointed out here that our (invalid) assumption of a uniform background intensity has probably also reduced the initial temperature of the gas, because, as the energy of reionization is deposited in the gas, the neutral fraction remains high making line cooling very efficient. In reality, the reionization would occur in expanding HII regions around discrete sources, so every element of gas is reionized during a very short time as it is engulfed by an expanding HII region, and the energy of all the photoionizations can be more efficiently preserved in the form of thermal energy for the gas.

We model galaxy formation as in Cen & Ostriker (1992, 1993a,b). The material turning into collisionless particles as “galaxies” is assumed to emit ionizing radiation, with two types of spectra: one characteristic of star formation regions and the other characteristic of quasars, with efficiencies (i.e., the fraction of rest-mass energy converted into radiation) of $e_{UV,*} = 5 \times 10^{-6}$, and $e_{UV,Q} = 6 \times 10^{-6}$, respectively. We adopt the emission spectrum of massive stars from Scalo (1986) and that of quasars from Edelson and Malkan (1986). Details of how we identify galaxy formation and follow the motions of formed galaxies have been described in Cen & Ostriker (1993a). Note that in the simulations which we are using in this paper no supernova energy input into IGM is included; we will study this effect in a later paper.

The resulting spectrum of the ionizing radiation field is shown in Figure 1 for the L10 simulation at redshifts $z = 2, 3$ and 4 , and for the L3 and L13 simulations at $z = 3$. In general, the results in this paper will be shown at this same set of redshifts for the L10 simulation, and only at $z = 3$ for the

TABLE 1: FRACTION OF BARYONS IN STARS

Simulation	z	Fraction
L10	2	0.086
L10	3	0.063
L10	4	0.042
L3	3	0.071
l3	3	0.060

other simulations, since this is enough to compare the results and see the effects of the large-scale power and the resolution. The intensity of the radiation depends mainly on the fraction of baryons which have been turned to stars in each simulation. This fraction is given in Table 1. In general, a higher fraction of baryons are turned into stars in the high-resolution simulation, but this fraction is also increased by the large-scale power included in the L10 simulation. We need to keep in mind, however, that the fraction of baryons in “stars” is only an indication of the gas that has collapsed to very high densities, but much of this gas might not turn into stars and remain in the form of gaseous disks. This is in fact probably the case, given the large amount of neutral gas that is observed in the damped systems.

HKWM and Katz et al. (1995) adopted a fixed model for the ionizing background in their simulation, and required an intensity of only $10^{-22} \text{ erg cm}^{-2} \text{ s}^{-1} \text{ Hz}^{-1} \text{ sr}^{-1}$ at the Lyman limit, which was necessary to reproduce the observed number of lines in the Ly α forest. They also adopt a specific spectral form $J_\nu \propto \nu^{-1}$ whereas we adopt a source function S_ν and, with allowance for absorption and cosmological expansion, compute J_ν as a function of time. We show for comparison the spectral shape adopted by HKWM and note that their assumed spectrum is much “harder” in the range $13.6 \text{ eV} < E < 54 \text{ eV}$ relevant for hydrogen and “softer” thereafter than is ours. As we shall see, we will need to adopt a low intensity of the background, similar to HKWM, and recalculate the neutral fractions for this lower intensity. With the intensity that we obtain in the simulation shown in Figure 1, there would be too few lines in our simulated spectra (our statement in Paper I that a high intensity could reproduce the number of observed lines was due to an error of a factor of three in computing the number of lines per unit redshift, plus the fact that lines were counted in real space instead of simulated spectra). In Katz et al. (1995), it was assumed that all the dense and cooled gas would remain in the form of neutral atomic material, with no stars being formed. It is interesting to notice that the fraction of baryons in the damped systems in their simulation is similar to the fraction of baryons that are turned into stars in ours.

3. PHYSICAL CONDITIONS OF THE ABSORBING SYSTEMS

In this Section, we analyze the nature of the structures formed in the simulations and we show some representative examples of the absorption spectra that are produced, and the physical

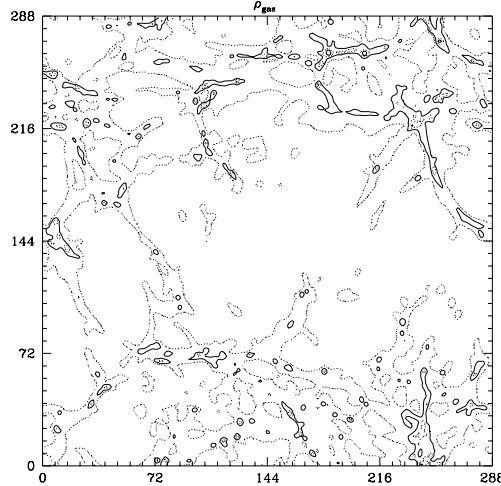


Figure 2a

Fig. 2: Slice of the $10h^{-1}$ Mpc simulation, averaged over 48 cells, showing contours of (a) gas density, where contours are at $\rho/\bar{\rho} = 10^{0.5(i-1)}$, $i = 1, 2, 3, \dots$, with solid contours for even i and dotted contours for odd i ; (b) dark matter density, with the same contours; and (c) neutral column density, with contours $10^{12+0.5i} \text{ cm}^{-2}$, $i = 1$ shown dotted and $i = 2, 3, \dots$ shown solid. The neutral column density is for J_{HI} as obtained in the simulation (Table 1), but we use $J_{-21} = 0.1$ in the rest of the paper to obtain a higher neutral density and similar Ly α absorption as observed.

conditions in the objects yielding absorption lines of different column densities. We shall concentrate on the simulation in the $10h^{-1}$ Mpc box (L10), since the larger size of this simulation allows us to have a more representative set of collapsed objects and, as we shall see, the inclusion of the large-scale waves which are absent in the simulations on the $3h^{-1}$ Mpc box has highly noticeable effects, whereas the corresponding loss of resolution in the large box has little effect on the systems causing the Ly α forest.

3.1. General Characteristics of the Absorbing Structures

Figures 2(a,b,c) show a slice of the L10 simulation with a thickness equal to 48 cells. The projected quantities shown are the gas density, the dark matter density, and the column density of neutral hydrogen. The first two quantities are averaged over the projected cells. Contours are shown for $\rho/\bar{\rho} = 10^{0.5(i-1)}$ ($i = 1, 2, 3, \dots$), where ρ is the density and $\bar{\rho}$ the average density of gas and dark matter for Figures 2(a,b), respectively. The contours are plotted as solid lines for even i , and as dotted lines for odd i . Figure 2c shows the integrated column density of neutral gas. Contours are shown at column densities $10^{12+0.5i} \text{ cm}^{-2}$, $i = 1$ with the dotted line and at $i = 2, 3, \dots$ with solid lines. As we shall see below, in order to reproduce the observed number of lines and average depression of the flux due to the Ly α forest, the density of neutral gas in the simulation has to be multiplied by a factor $\sim 15 - 20$, which can be achieved by either lowering the intensity of the

ionizing background in the simulation by this factor, or raising the baryon density by the square root of this factor.

The distribution of dark matter and gas on large scales follows the interconnected structure of sheets, filaments and halos that is produced in any hierarchical gravitational collapse theory. The gas and dark matter follow each other very well on large scales. However, on small scales the dark matter is very clumpy, showing the small structure of small halos that collapsed at an earlier epoch and are now merging, whereas the gas is much smoother. In particular, the central density of spheroidal structures (halos) is much higher in dark matter than in gas. This is due to the gas pressure, which prevents it from collapsing on scales smaller than the Jeans length, $\lambda_J \equiv c_s(\pi/G\bar{\rho})^{1/2}$, where c_s is the sound speed of the gas (e.g., Peebles 1980, §16). At $z=3$, and for a gas temperature $T = 15000$ K ($c_s = 19$ km s $^{-1}$), the Jeans length in our model (with $\Omega = 0.4$ at $z = 0$) is $\sim 800h^{-1}$ kpc in comoving scale, which is 23 cells in the simulation. The smallest structures where the gas will start to collapse will be on this scale, and the photoionized gas remains smooth over the Jeans length, which decreases in high density regions as $\rho^{-1/2}$. There are numerous very small structures (size of 1 to 3 cells in projection) in the dark matter slice showing a contour level of $\rho/\bar{\rho} = 1$. These structures are partly due to the discreteness and small number of dark matter particles involved (a projected cell with density equal to the mean density contains only six particles).

In Figures 3(a,b,c,d,e), we show the gas density in five slices of one cell thick. The contours are the same as in Figures (2a,b) ($\rho/\bar{\rho} = 10^{0.5(i-1)}$, $i=1,2,3,\dots$). The five slices shown are separated by 9 cells, or $78h^{-1}$ kpc; Figure 2 is averaged over 48 cells. A filamentary structure located near the bottom of Figure 3a connecting northwest-ward to the halo at position (72,72) is clearly seen to extend through all five slices. Another inter-connected structure located at the top right corner is also seen in five slices. The thin structures shown as the contour level equal to the mean density typically are sheet-like, which gradually turn into filaments as density levels go higher, and finally become spheroids in the vertices, the likely sites for formation of galaxies. The typical objects collapsing in the simulation at this redshift form from regions of $\sim 1h^{-1}$ Mpc, containing total masses of $10^{11}h^{-1} M_\odot$ (for $\Omega = 0.4$), and should therefore be the progenitors of relatively low-mass galaxies.

The gas density in a slice of the L3 simulation, in the $3h^{-1}$ Mpc box, is shown in Figure 4. This slice is also one cell thick and the density contours are the same as in Figure 3. The only regions where the density is varying on a small scale are the halo centers, where the density is highest. Filamentary structures are already well resolved in the L10 simulation. The gas is intrinsically smooth in such regions due to its own pressure. The characteristic thickness of these structures is also an intrinsic physical property, independent of the box size: $\sim 250h^{-1}$ kpc in comoving scale. The characteristic thickness of the structures is related to the scales that are collapsing at a given epoch, in a similar way as the thickness of the filaments of the large-scale distribution of galaxies is related to the scales from which clusters are collapsing at the present epoch.

We now take the lower half of Figure 3b to examine it in more detail. In Figure 5, we show contours of the density, temperature and velocity divergence of the gas in this half slice. The gas density (upper panel) is the same as that shown in the lower half of Figure 3b, but with more contours. The solid contours are shown for $\rho/\bar{\rho} = 10^{0.25(i-1)}$ ($i = 1, 2, 3, \dots$); the dotted contour is for $\rho/\bar{\rho} = 10^{-0.25}$. The middle panel shows the temperature with solid contours for $T = 10^{4.2+0.1i}$ K, $i = 1, 2, 3, \dots$, and the dotted contour for $T = 10^{4.2}$ K. The bottom panel shows

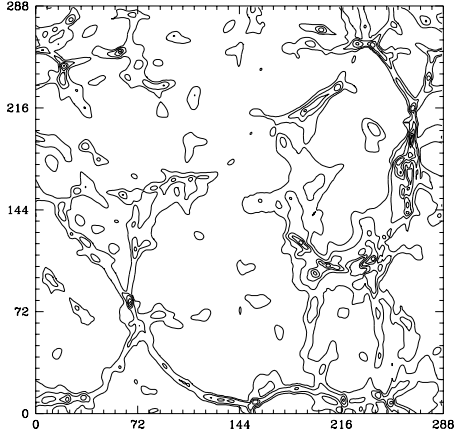


Figure 3a

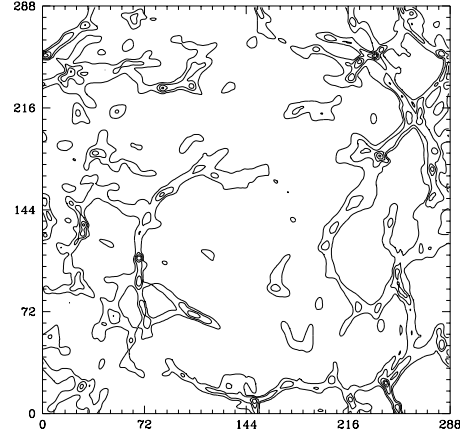


Figure 3b

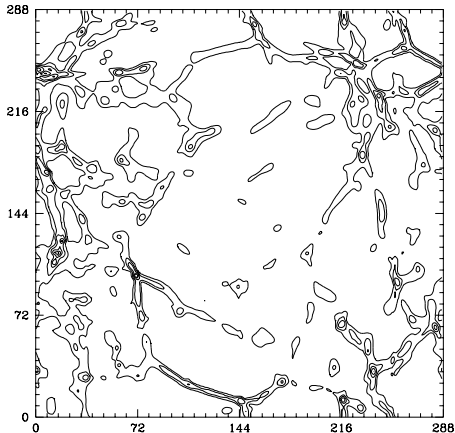


Figure 3c

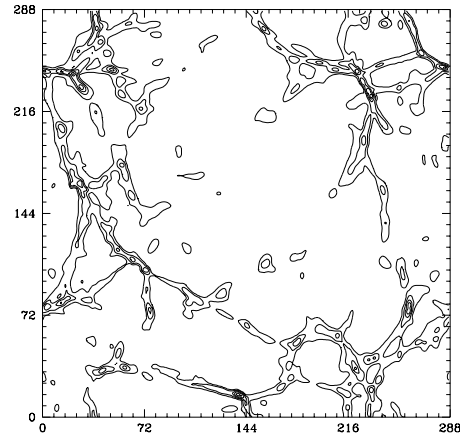


Figure 3d

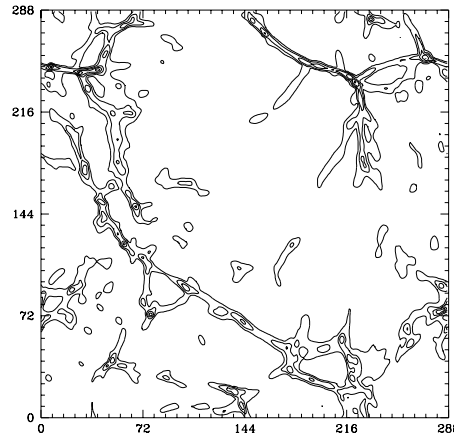


Figure 3e

Fig. 3: Gas density in five slices with thickness of only one cell, (numbers 4,13,22,31, and 40 among the 48 of Fig. 2), with the same contours as in Fig. 2a but all shown in solid curves. The separation between two consecutive slices is 78^{-1}kpc in proper units.

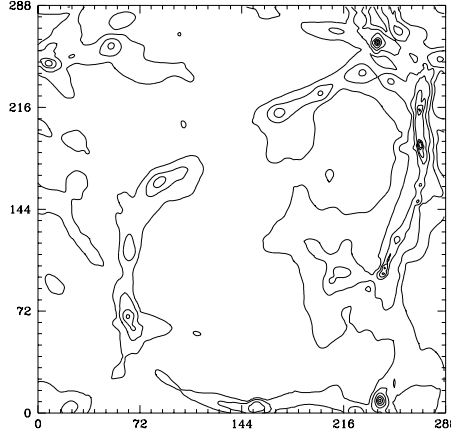


Figure 4

Fig. 4: Slice of one cell showing gas density in the L3 simulation, with the same contours as in Fig. 2.

Fig. 5: (a) Lower half of the slice in Figure 3b is shown with contours at $\rho/\bar{\rho} = 10^{0.25(i-1)}$, $i = 1, 2, 3, \dots$ for solid contours and $i = 0$ for dotted contour. (b) Temperature contours at $10^{4.2+0.1i}$ K, $i = 1, 2, 3, \dots$ for solid contours and $i = 0$ for dotted contour. (c) Peculiar velocity divergence contours at $\nabla \cdot \mathbf{v}_p = -3H$ (solid contour, corresponding to constant proper density), and $\nabla \cdot \mathbf{v}_p = 0$ (dotted contour, corresponding to constant comoving density).

contours of peculiar velocity divergence, with $\nabla \cdot \mathbf{v}_p = 3Hi$, ($i = 0, -1$), where H is the Hubble constant of the model at $z = 3$. The first contour ($i = 0$) is shown as dotted, and it indicates the regions expanding at the Hubble rate (i.e., where the comoving density stays constant). Regions outside this contour are expanding faster than the Hubble rate, and are typically in voids and low-density regions of sheets and filaments. The solid contour ($i = 1$) is in stationary regions, with constant proper density.

In the relatively dense regions along sheets or filaments, a double shock is often formed. Initially, the pressure rises in the center, and then two shock fronts emerge and separate with increasing velocity, so the gas is heated to progressively higher temperatures as the infall velocity increases, causing generally a temperature minimum between the shocks (see Sunyaev & Zel'dovich 1972). The middle panel shows the shock heated gas as on mesa like plateaus with sharp boundaries indicating the outward propagating shocks. The double shock structure is seen along several of the filaments, in the velocity divergence contour map as two parallel peaks. The fact that the gas is photoionized implies that it starts with an initial entropy, and that when the infall velocities are small the collapse of the gas can be stopped by its own pressure. The shocks are formed later, when the velocities are high enough, but they are generally weak (i.e., the shock velocities are of order or only a few times the sound speed of the gas), and the temperature minimum between the double shocks is often very small or non-existent (notice, though, that very thin slabs of gas in thermal equilibrium with the radiation might be present and not be reproduced with our resolution). In low-density regions along

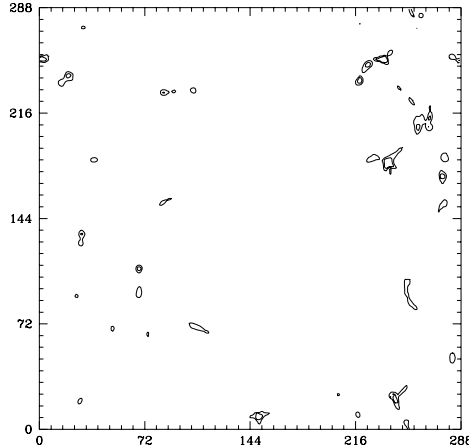


Figure 6

Fig. 6: Contours of cooling time in the same slice as Figure 3b, for $t_{cool} = 10^{-0.5i} H^{-1}$, $i=0,1,2,\dots$

the filaments, the gas expands as it falls towards higher density clumps, and it can also expand into the voids as the ram-pressure of infalling material declines. At some point, the shocks surrounding the filament may become pressure waves. In fact, several examples can be seen in Figure 5 where the expansion rate across a thin filament has two minima around the center, but the gas is not contracting anywhere. Some of these low-density objects are isolated within voids (as the small density enhancement towards the center of the panels in Figure 5); they probably correspond to structures below the Jeans scale where the gas is never shocked and it can bounce back from the dark matter potential well due to its own pressure. In this case, the gas should probably experience a damped oscillation around the dark matter, although on average it expands as the surrounding gas density in the void declines. The details of these processes and the distinction between weak shocks and pressure waves is difficult to see in the simulation owing to the limited resolution; this will be examined in more detail in Gnedin et al. (1995) for the case of a uniform, plane-parallel sheet or filament.

We also see that the lowest temperature gas occurs in the voids, and the gas is generally hotter in the high density regions owing to adiabatic and shock heating, except for the features caused by double shocks and cooling mentioned before. The gas in filamentary structures is generally expanding in proper coordinates, except at the shocks, but the overdensity still rises (in other words, the gas contracts in comoving coordinates). As expected, the rate of contraction increases towards high density regions.

As the gas continues to collapse along filaments, it is shocked again as it merges into halos and will typically go through a complicated history of radiative cooling and shock heating. In Figure 6 we show the following contours of the cooling time: $t_{cool} = 10^{-0.5(i-1)} H^{-1}$, $i = 1, 2, 3, \dots$, in the same slice as in Figure 3b. The high density regions are cooling over timescales much shorter than the Hubble time. As the gas cools and contracts in these regions, small inhomogeneities will grow and lead to the formation of clouds photoionized by the ionizing background and pressure-confined

by the surrounding hot gas (e.g., Fall & Rees 1985). This is probably the first physical process affecting the photoionized gas which our simulation is not able to adequately resolve. In any case, the cooled gas should continue to fall to the halo center and form galaxies. The high column density absorption systems that can arise in this situation have been studied by Katz et al. (1995) in an SPH simulation, under the assumption that all the gas accreting to the center remains in the form of neutral, atomic gas.

3.2. Choice of the Ionizing Radiation Intensity

The density of neutral gas shown in Figure 2c depends on the assumed intensity of the ionizing radiation field used in the simulation. Most of the gas in the simulation is at low enough density and temperature that photoionization dominates over collisional ionization, and so if the intensity of ionizing photons is increased by some factor, the neutral density would simply decrease by the same factor everywhere. This will alter the number of absorption lines at a fixed column density that will be observed along a line of sight, and the average absorption decrement implied by all the neutral gas. The intensity is determined by the models of production of ionizing photons from the gas particles that form stars (see §2). The value obtained for the intensity depends on an arbitrary parameter of the models that were used giving an efficiency of production of UV photons that can escape from stars and quasars formed out of the radiatively cooled gas. The redshift evolution of the intensity can also vary depending on the rate at which the stars and quasars form. Since the detailed physics determining these processes are unknown to us, we can change the photoionization rate to a value that will imply an average flux transmission in the Ly α spectra close to what is observed.

For the purpose of determining the neutral fraction, the important quantity is the photoionization rate. We define the quantity J_{HI} as

$$J_{HI} \equiv [\bar{\sigma}_{HI}]^{-1} \int_{\nu_{HI}}^{\infty} \frac{d\nu}{\nu} J(\nu) \sigma_{HI}(\nu), \quad \bar{\sigma}_{HI} \equiv \int_{\nu_{HI}}^{\infty} \frac{d\nu}{\nu} \sigma_{HI}(\nu), \quad (1)$$

where $\sigma_{HI}(\nu)$ is the ionization cross section of HI, and ν_{HI} is the frequency of the ionization potential. This is proportional to the photoionization rate, but is expressed in the usual (cumbersome) units in the literature. In this paper, we shall fix this value to $J_{HI} = 10^{-22} \text{ erg cm}^{-2} \text{ s}^{-1} \text{ Hz}^{-1} \text{ sr}^{-1}$ at all redshifts (this corresponds to a photoionization rate of $4.34 \times 10^{-13} \text{ s}^{-1}$). As we shall see, this value will give us a number of absorption lines and an average flux decrement due to Ly α absorption close to what is observed.

The values of J_{HI} that were obtained from the emission models in various simulations at different redshifts are given in Table 2. We see that these values of J_{HI} are much higher than the value we need to assume to have the right amount of absorption. This probably indicates that the sources of ionizing photons should be fainter than were assumed, and also that the absorption is higher. A lower J_{HI} would imply an increase in the neutral fraction of all the systems, and therefore an increase of the absorption. In addition, optically thick systems are not treated adequately here, and, as we shall see, their numbers in our simulation are below the observed ones, so the absorption should be strongly increased relative to our model. It is also likely that the sources of ionizing photons appear in dense regions where the absorbers are located, further reducing the background intensity. An intensity $J_{-21} = 0.1$ ($J_{-21} \equiv J_{HI} / (10^{-21} \text{ erg cm}^{-2} \text{ s}^{-1} \text{ Hz}^{-1} \text{ sr}^{-1})$) is also significantly lower

TABLE 2: RADIATION INTENSITY

Simulation	z	J_{-21}
L10	2	0.97
L10	3	1.56
L10	4	0.76
L3	3	1.38
13	3	0.83

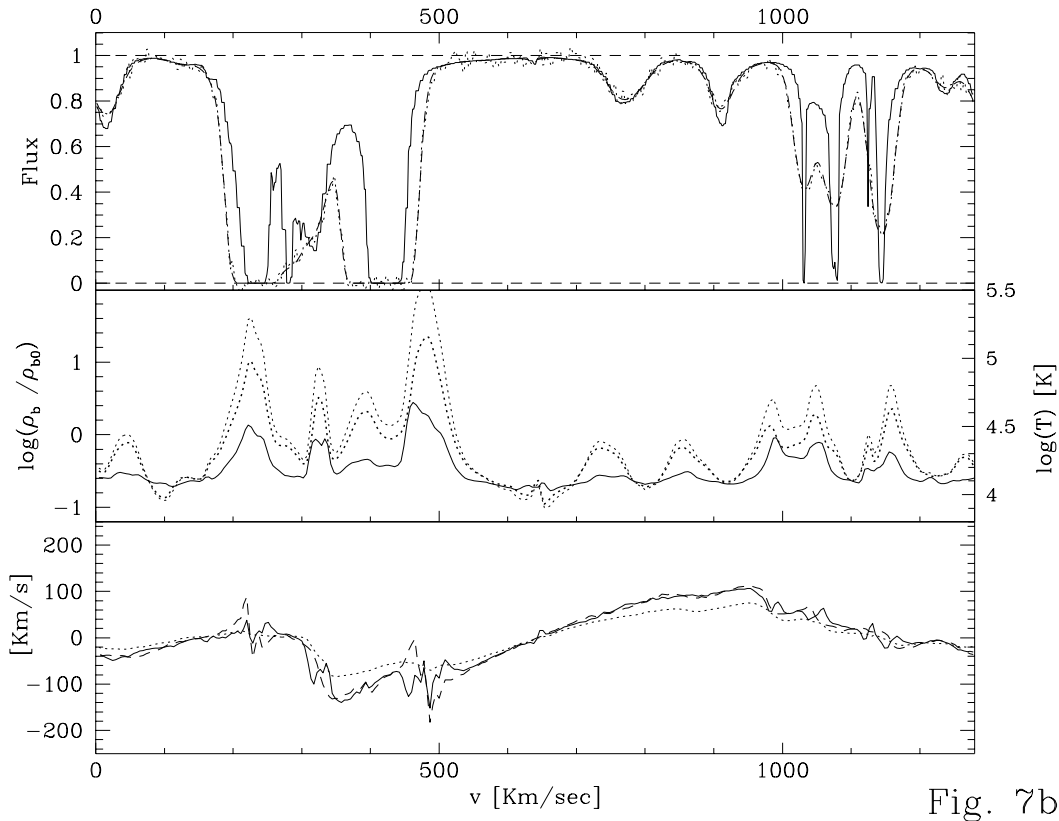
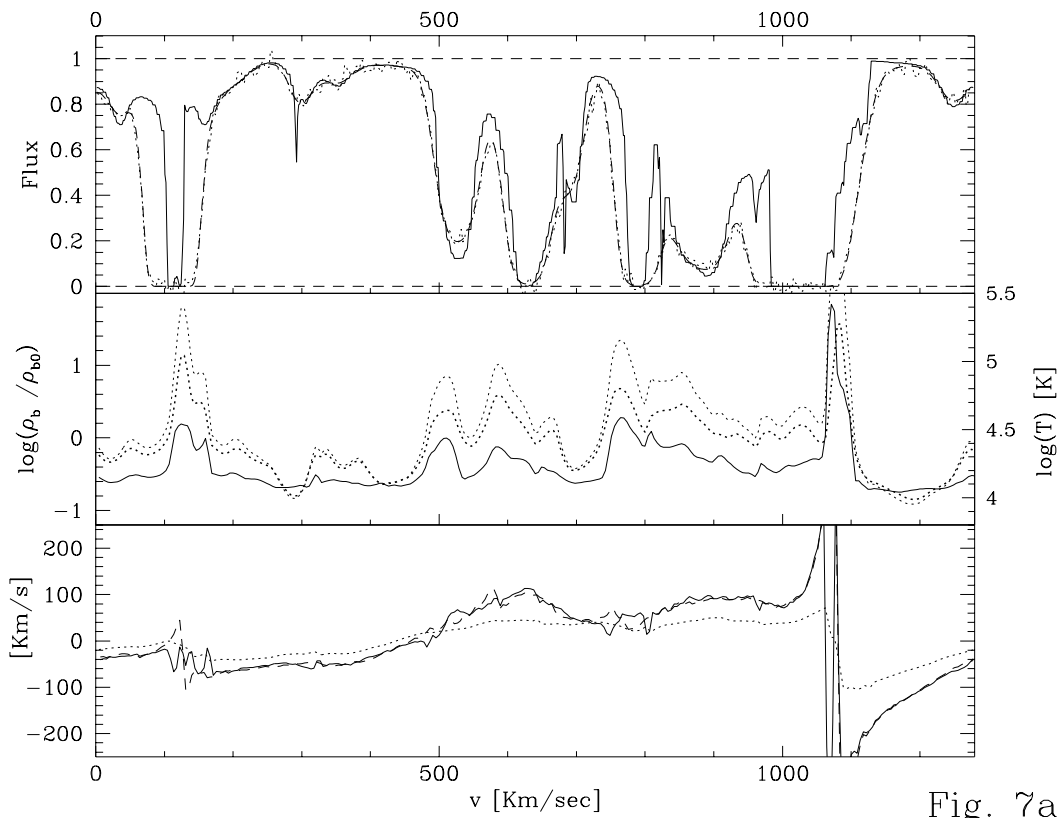
than the estimated contribution of the observed quasars, and the values given by measurements of the proximity effect. However, the same neutral densities can be obtained by raising Ω_b for a higher J_{HI} ; this will be discussed in detail in §5. The neutral fractions in the simulation have been recalculated for the new value of the photoionization rate, including also collisional ionization. These neutral fractions are used for all the results shown in this paper (except Fig. 2c), instead of the ones computed as the simulation was evolved.

3.3. Examples of Simulated Spectra

We now select several rows along the half slice we have described, to see the absorption lines that are produced. We take four horizontal rows from the slice in Fig. 5 with cell number on the vertical axis equal to 20, 70, 96, and 133, indicated by the four horizontal dashed lines in each panel. For each row we plot three panels in Figures 7(a,b,c,d). The middle panels show the density along the row as the thick dotted line, and the temperature as the solid line. The thin dotted line is the pressure, plotted on the same scale as the density but with arbitrary units. The coordinate along the row is shown as a velocity, where the proper coordinate is $x \equiv v/H$ ($H = 512h \text{ km s}^{-1} \text{ Mpc}^{-1}$ at $z = 3$ in our CDM+ Λ model). The total length in velocity of the L10 simulation at $z = 3$ is 1280 km s^{-1} , and a cell corresponds to 4.44 km s^{-1} . The peaks in density and temperature seen along these rows can easily be identified in the contour plots of Figure 5.

The peculiar velocity of the gas along the row is shown as the dotted line in the lower panel. We compute the resulting spectrum in the same way as was done in Paper I; we use equations (1) and (2) of Miralda-Escudé & Rees (1993). The solid line in the upper panel shows the spectrum without including thermal broadening, and the dashed line includes thermal broadening. Finally, the dashed line in the lower panel shows the gravitational acceleration divided by the Hubble constant, $-(\nabla\phi)/H$, and the solid line shows the total acceleration $-(\nabla\phi + \nabla p)/H$ (notice that this acceleration gives the time derivative of the *peculiar* velocity, since the gravitational potential due to the average density is subtracted out). Regions where the acceleration is increasing to the right are being forced to expand in comoving coordinates, while they are being forced to contract in comoving coordinates when the acceleration decreases to the right.

3.3.1. Nature of the Absorption Features



We see in Figure 7 that, generally, the absorption features in the spectra are caused by density peaks along a row. Velocity caustics tend to produce narrow features when thermal broadening is not included, but these are smoothed out by the thermal velocities. Usually, the dynamical structure of the objects causing the absorption lines consists of two shocks surrounding the central density peak, as mentioned above. This is seen in the variation of the total acceleration (solid line in the lower panel) as we move across an object: on the left side, there is usually a large negative peak, corresponding to the infalling gas being stopped on a shock. The same thing occurs on the right side, with a positive peak in the total acceleration. In the region between these two shocks, the total acceleration can show a variety of different behaviors, indicating sometimes the presence of other shocks. In general, the variation of the total acceleration within the two shocks is less than the gravitational acceleration, showing a tendency for pressure gradients to balance gravity; however, gas motions are always important. In any case, these regions are not very well resolved by our code, since often there are only a few cells between the two bounding shocks in any given structure.

As seen in Figure 5, most of the objects giving rise to absorption lines are sheets and filaments where the gas continues to fall to denser regions in halos. The object on the lower left corner of Figure 5, producing the first absorption line on the left edge in Figure 7a, seems to have a more spherical nature, but it is actually an edge-on filament. The weaker absorption lines tend to be produced by small density enhancements in the voids (e.g., the small object towards the center of Fig. 5, causing the absorption line at $v = 750 \text{ km s}^{-1}$ of the spectrum in Fig. 7c). These correspond to potential wells where the velocities are too low for the gas to be shocked. The smooth pressure variation of the photoionized gas is sufficient to stop the collapse, and the gas pressure oscillates in a wave. In this case, the gas density can never reach very high values until there is a merger with a higher velocity structure.

Voids are common features in the simulations. They are typically underdense by factors of a few; density maxima along them, which may not reach the mean density, are still visible in absorption resembling absorption lines as they stand out from the even lower background density. In the spectra they tend to appear as low column density $N_{HI} \sim 10^{13} \text{ cm}^{-2}$ relatively broad features. Variations in the density of voids should also cause weak large scale differential absorption, which could be difficult to detect in real data as polynomial fits to apparently line free regions of the spectrum are used to determine the continuum of the QSO.

3.3.2. Line Profile Analysis

We now present the results of applying the same procedure used to analyse observations of the absorption lines to the examples of absorption spectra that we have shown. This analysis will be carried out further over a large sample of the simulated spectra in Rauch et al. (1995). In Table 3 we give the result of Voigt profile fits to the four spectra in Figure 7. The spectra were created by emulating typical datasets obtained with the Keck telescope high resolution spectrograph, by convolving them with a velocity resolution of 8 km/s (FWHM) and adding noise with a S/N per pixel of 50. The fitting procedure was identical to the one used previously on real data (Carswell et al. 1991), except that here each simulated spectrum is short enough to be treated as a single fitting region. This has the advantage that we do not need to decompose in advance the spectrum into several regions chosen on the basis of statistically significant continuum depressions, a procedure

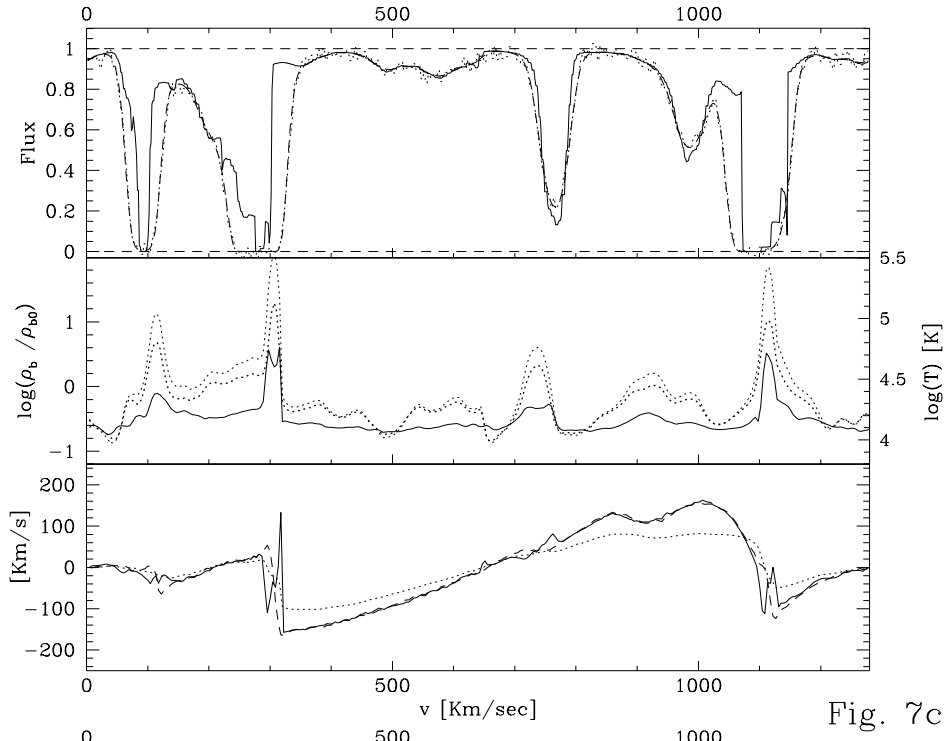


Fig. 7c

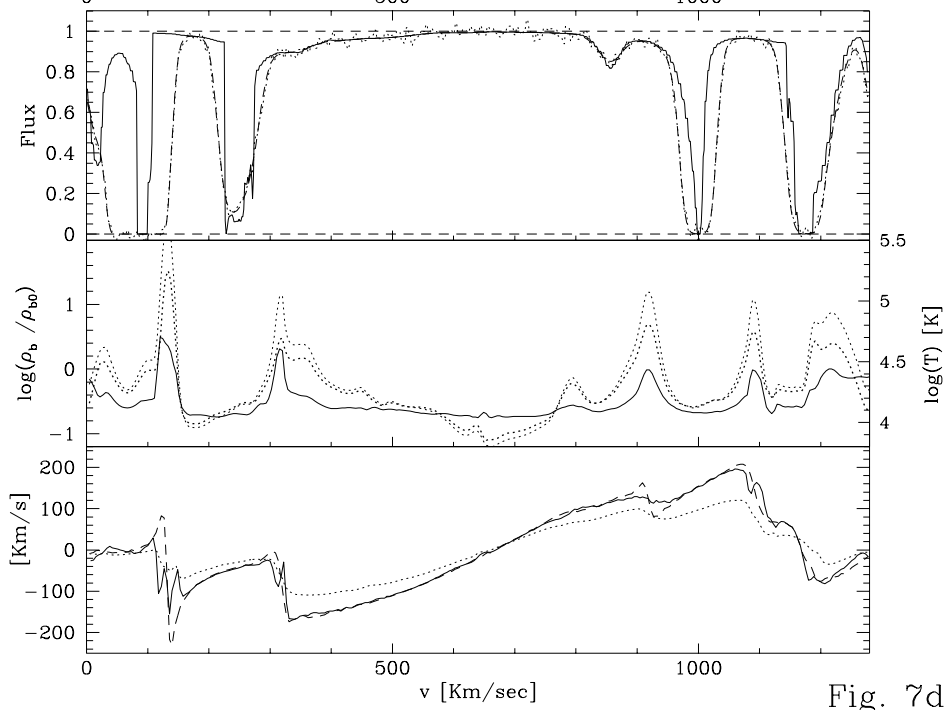


Fig. 7d

Fig. 7: Middle panel in each figure shows the gas density along a row, in units of the average gas density (thick dotted line; left vertical axis), the gas temperature (solid line; right vertical axis), and the gas pressure (thin dotted line; the same scale as density but arbitrary units). Spatial coordinate in horizontal axis is $x = v/H$. Rows shown in Figs. 7(a,b,c,d) are marked as dashed lines in slice in Fig. 5. Calculated Ly α absorption spectrum is in top panel, without thermal broadening (solid line), and including it (dashed line). Peculiar velocity is shown as dotted line in bottom panel, together with gravitational acceleration (dashed line) and total acceleration (solid line) divided by the Hubble constant.

TABLE 3: ABSORPTION LINE PARAMETERS

#	v [km/s]	b	±	$\log N_{HI}$	±
Fig. 7a (z = 3)					
1	34.1	32.1	4.2	13.06	0.11
2	109.6	21.8	0.5	15.06	0.04
3	139.3	63.2	10.0	13.41	0.17
4	295.2	20.4	2.0	12.72	0.09
5	343.4	45.9	8.1	12.84	0.08
6	434.6	23.7	8.3	11.96	0.14
7	526.1	34.2	0.4	13.89	0.00
8	626.4	27.6	1.2	14.13	0.04
9	650.1	50.5	2.2	13.72	0.14
10	693.2	20.8	2.8	13.10	0.15
11	788.1	25.0	0.4	14.33	0.02
12	856.9	37.6	8.7	13.98	0.15
13	899.2	27.5	2.5	13.86	0.17
14	1021.1	53.3	0.5	14.96	0.01
15	1150.0	65.9	37.6	12.48	0.21
16	1244.7	28.7	2.8	12.88	0.06
Fig. 7b (z = 3)					
1	15.0	24.8	1.7	12.94	0.06
2	119.0	11.7	8.5	11.52	0.31
3	229.0	22.6	0.5	14.84	0.05
4	274.7	59.3	0.9	14.27	0.01
5	353.5	202.1	19.5	13.34	0.07
6	412.3	25.6	0.3	15.66	0.04
7	770.5	37.3	1.8	12.99	0.03
8	920.3	23.8	1.2	12.86	0.03
9	946.3	153.7	77.8	12.91	0.18
10	1030.0	18.2	0.4	13.32	0.01
11	1073.6	21.3	0.6	13.49	0.02
12	1142.5	19.7	0.4	13.61	0.01
13	1225.0	104.2	59.8	12.87	0.12
14	1236.2	18.6	4.0	12.38	0.19

which is generally not done according to an automatic, well defined algorithm when lines are severely blended.

The absorption line width arises from both hydrodynamic and thermal motions; the relative contributions vary substantially among the absorption lines, as seen in Fig. 7. The contributions are difficult to disentangle as the temperature across a collapsing structure is not constant and the infall of gas often is not symmetric about the density maximum. The temperature in the densest

TABLE 3: ABSORPTION LINE PARAMETERS - CONTINUED

#	v [km/s]	b	±	log N_{HI}	±
Fig. 7c (z = 3)					
1	91.4	21.7	0.2	14.18	0.01
2	144.3	14.6	2.7	12.28	0.08
3	244.0	65.8	3.3	13.88	0.05
4	277.7	24.8	0.6	15.06	0.04
5	379.6	49.5	37.6	12.31	0.46
6	482.3	30.5	3.4	12.59	0.06
7	575.9	61.8	3.1	13.08	0.02
8	713.0	24.3	9.0	12.15	0.17
9	763.6	25.6	0.3	13.72	0.01
10	850.1	31.6	11.9	12.02	0.12
11	913.5	20.7	2.9	12.39	0.06
12	984.4	35.6	0.6	13.51	0.01
13	1084.9	28.2	0.6	14.54	0.06
14	1128.0	20.7	1.6	13.75	0.11
15	1226.6	78.7	34.1	12.75	0.23
16	1273.7	24.2	17.3	12.04	0.64
Fig. 7d (z = 3)					
1	17.0	21.6	1.2	13.28	0.04
2	82.7	23.9	0.3	15.71	0.04
3	229.8	17.7	2.1	13.44	0.22
4	252.0	26.7	2.8	13.76	0.11
5	326.2	54.5	9.8	12.91	0.07
6	419.1	23.5	10.1	11.97	0.27
7	491.6	58.0	12.4	12.48	0.08
8	853.1	18.7	4.5	12.37	0.21
9	861.4	53.3	15.9	12.70	0.09
10	976.6	37.7	4.2	13.02	0.20
11	998.2	19.9	0.5	14.30	0.01
12	1174.3	23.6	0.3	14.29	0.01
13	1216.2	276.0	62.3	13.26	0.05
14	1216.6	22.9	2.8	13.06	0.09

regions is generally higher than the thermal equilibrium temperature for photoionized gas, due to shock heating. The combination of such high temperatures and the hydrodynamic motions can explain the observed large b-parameters, which would imply unrealistically low densities if thermal equilibrium was assumed (e.g., Press & Rybicki 1993).

There are several lines with small bulk motion (as apparent from the comparison of the thermally broadened and unbroadened profiles), and in these cases the Doppler parameter values correspond

TABLE 3: ABSORPTION LINE PARAMETERS - CONTINUED

#	v [km/s]	b	±	log N_{HI}	±
Fig. 8a (z = 2)					
1	18.4	33.0	8.3	12.47	0.10
2	96.5	21.7	0.4	14.14	0.02
3	128.4	35.0	13.6	12.77	0.37
4	232.4	23.8	4.7	12.07	0.08
5	294.7	9.2	8.2	11.28	0.29
6	421.4	26.7	0.3	13.36	0.01
7	594.2	41.5	2.7	12.74	0.03
8	696.3	326.4	60.5	12.97	0.06
9	725.7	23.6	0.3	13.45	0.01
10	881.6	21.1	0.8	13.10	0.02
11	937.7	28.9	0.2	14.21	0.01
12	1089.3	23.2	2.7	12.49	0.08
Fig. 8b (z = 4)					
1	1.9	60.0	21.4	13.65	0.25
2	44.4	24.7	1.6	13.78	0.08
3	118.2	20.3	0.6	16.00	0.12
4	157.2	79.9	4.0	14.02	0.04
5	252.7	17.0	2.3	12.47	0.08
6	355.4	19.0	0.3	13.61	0.01
7	398.2	24.8	0.7	13.51	0.01
8	473.2	132.5	8.6	13.57	0.03
9	580.8	28.7	1.6	14.00	0.08
10	609.7	20.6	1.2	14.00	0.09
11	722.8	19.2	0.7	15.42	0.12
12	756.3	122.8	2.8	14.43	0.01
13	823.9	20.0	0.6	14.68	0.05
14	978.9	35.4	0.6	15.00	0.03
15	1086.4	33.7	2.6	14.56	0.03
16	1187.5	25.1	0.4	16.16	0.07
17	1314.6	75.1	57.6	13.09	0.50

to temperatures that are close to the peak temperature in the system, usually occurring in the region of highest density. See, for example, the first strong line in Fig. 7a (second line in Table 3). High temperatures like that of the strong line at $v \simeq 1000 \text{ km s}^{-1}$ in Fig. 7a are usually detected as such, although with a larger error due to additional broadening by infall of gas. Often, however, the line profile of intermediate or lower column density systems is dominated by bulk motion (e.g., the lines in the center of the spectrum in Fig. 7c). The weakest lines have widths dominated by bulk motion, and they are produced by intergalactic gas in expansion. Despite the low gas temperature, these lines are usually not narrow due to the expansion velocities.

3.3.3. Departures from Voigt Profiles

As a consequence of the dynamical character of the clouds, we find numerous absorption lines which show departures from single Voigt profiles. Typically, such a system may contain some cool, dense gas producing a high column density, narrow component, and at the same time hotter gas recently shock-heated at high velocity, which will produce broad tails. Cooler and less dense gas falling into the system also contributes to such tails, often making them asymmetric. For example, the line at $v = 250 \text{ km s}^{-1}$ in Fig. 7d shows an extension to the right which is due to accreting gas, as seen in Figure 5. One can always obtain a good fit to such a line by using superposed Voigt profiles, although the added lines will not necessarily correspond to physically distinct “clouds”. These multi-component systems will give rise to a correlation of line properties. An individual system is often well represented by a pair of lines with a small velocity splitting, consisting of a narrow central component (cool gas) and a broader wing-like component caused by the hotter and/or infalling gas. From an analysis of a large sample of simulated spectra, we find that there is indeed a strong anticorrelation of Doppler parameters on small (order 10-20 km/s) scales, and there are indications that we are seeing it in real data as well; we shall present this in detail in Rauch et al. (1995).

3.3.4. Temporal Evolution

Finally, we show in Figures 8(a,b) the density, temperature and pressure of the same row as in Fig. 7a at $z = 2$ and $z = 4$, as well as the calculated spectrum. The most striking change with redshift is the increase of the average absorption, as in the observations. This is mostly due to the general increase of the optical depth corresponding to a fixed overdensity as $(1 + z)^{4.5}$ for a constant proper intensity J_{HI} (in the same way as the Gunn-Peterson effect). As we shall see below, most of the gas in the absorbers tends to be expanding at rates close to the Hubble rate, and the overdensities are increasing only slowly. In addition, the gas is also becoming hotter due to the increasing shock velocities as larger scales collapse, which further reduces the neutral fraction.

In addition to the average increase of the optical depth, the systems yielding absorption lines are evolving as they collapse gravitationally, with the gas becoming more overdense as it flows to denser regions, and the structures merging with each other. Transverse motions across the row are also responsible for changes (especially for the high column density systems, which vary over small scales). Thus, the evolution of an individual absorption system is difficult to interpret, but the spectra give an overall impression of the expected evolution with redshift of the general population of absorbers which seems to agree with what is observed. Most of the absorption systems can be traced from $z = 4$ to $z = 2$, as their column density decreases.

The fitted lines in Table 3 show a general decrease of the Doppler parameter with increasing redshift, in agreement with recent observations of redshift 4 QSOs by Williger et al. (1994) and Lu (1995, in preparation). The gas temperatures are in fact lower at high redshift, owing to the higher velocities and temperatures of the gas on the larger scales of collapse at lower redshifts (see §3.4). However, lower Doppler parameters might also arise spuriously due to the increased blending at high redshift.

3.4. Physical Conditions of the Absorbers

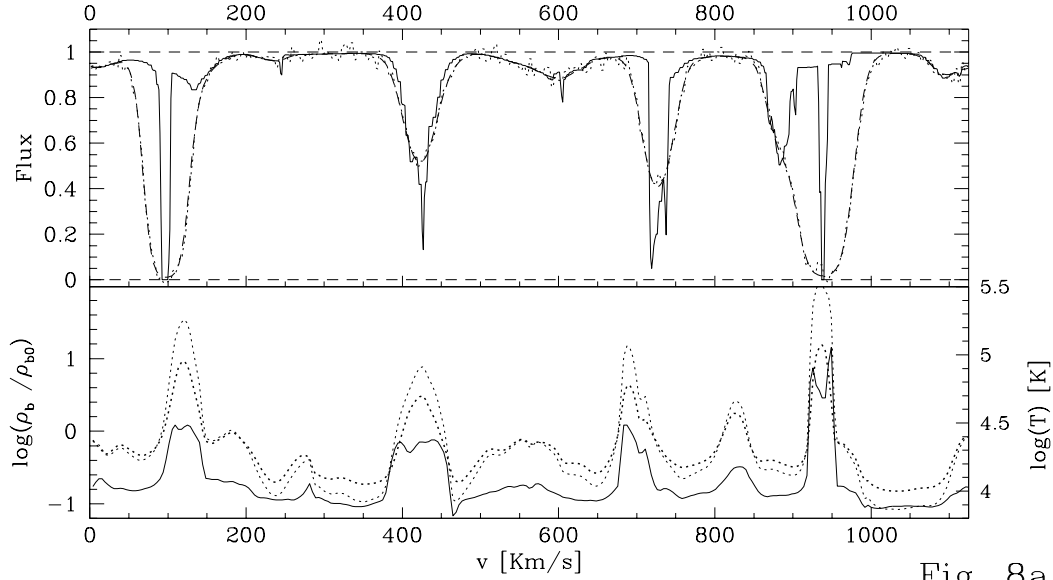


Fig. 8a

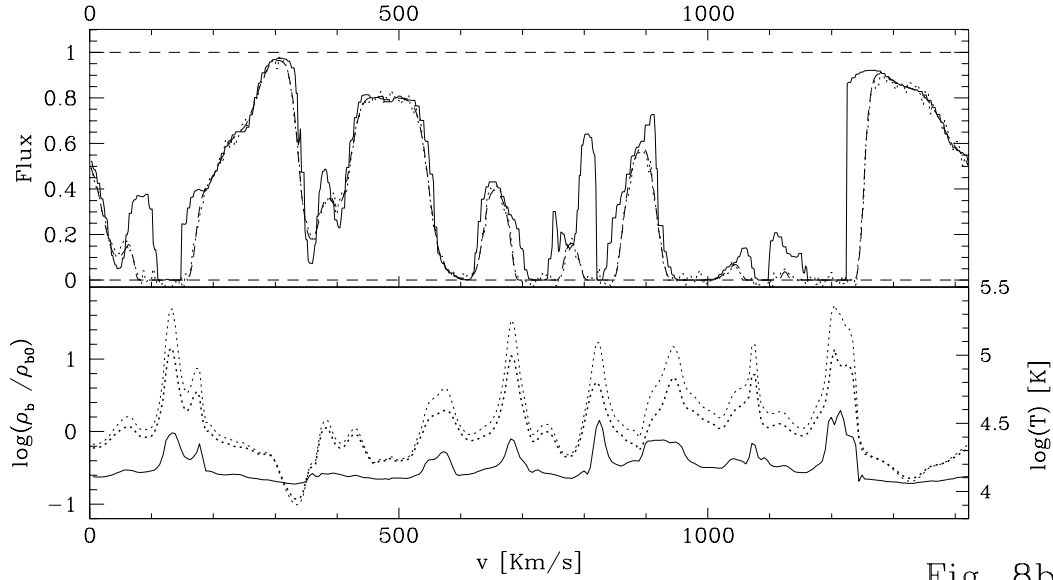


Fig. 8b

Fig. 8: Same as top and middle panels of the same row as Fig. 7a, at $z = 2$ (Fig. 8a) and $z = 4$ (Fig. 8b).

The gas yielding Ly α absorption is spread throughout all the volume in our simulation, and therefore there is no clear way to identify the gas belonging to a given “Ly α cloud”. However, the simulated spectra show absorption lines similar to the observed ones, so it seems useful to adopt a criterion to identify the objects producing these lines and analyze their physical state. Here, we shall identify clouds by choosing a contour in real space at a fixed neutral hydrogen density, and identifying each interval along a line of sight within the contour as a cloud. Our “clouds” are therefore

not three-dimensional entities, but regions which are defined only for one particular line of sight; a connected region in space above the neutral density of the contour could be disconnected along a line of sight crossing this region, and would therefore be split into several clouds. We measure the total and neutral column density along such clouds, and the neutral-weighted temperature, neutral fraction, and velocity divergence. We choose the contour having a neutral density corresponding to the value in photoionization equilibrium when the gas density is equal to the average baryon density and at a temperature $T = 10^4$ K. The distribution of neutral column densities obtained in this way will be shown later in §5; we shall also identify lines in the simulated spectra using an analogous procedure in §4.

Figure 9a shows the median value of the total column density, for clouds of a fixed neutral column density. The results are shown for the L10 simulation at three redshifts as thick lines, as indicated in the figure. At $z = 3$, we also show two thin dashed lines such that 5% of the systems have total column densities below the lower line, and 5% above the upper line. These two thin lines show that the dispersion of the total column density at a fixed neutral column density is very small (the dispersion is similar at other redshifts). The variation in column density corresponds mostly to a variation of the gas density. The dispersion is small because variations in pathlength for clouds of fixed column density are not too large, and they cause both column densities to change by the same factor, moving the location of a cloud in Fig. 9a in a direction only slightly steeper than the dependence of the median N_H on N_{HI} . Variations of temperature at a fixed gas density are also small.

The distribution of the neutral-weighted neutral fraction for lines of a given neutral column density is shown in Figure 9b (line types have the same meaning as in Fig. 9a). In Figure 9c, the distribution of the neutral-weighted temperature is shown in the same way, and the distribution of the neutral-weighted velocity divergence is shown in Figure 9d. Regions expanding at the Hubble rate have $\text{div } v_p = 0$, while regions with constant proper density have $(\text{div } v_p)/(3H) = -1$. These results have been obtained from 18000 random lines of sight (selected as described below, in §4.4) through the L10 box at each redshift, and measuring all the quantities for every “cloud” identified as explained above.

Higher column densities correspond to higher neutral fractions of hydrogen. Thus both increasing the total column density and increasing the neutral fraction combine together to produce the larger observed column densities of neutral hydrogen, as the gas density through a line of sight rises. If the median pathlength and temperature were constant for clouds of different column density, the neutral fraction should rise as $N_{HI}^{1/2}$, which is approximately the dependence seen in Fig. 9b. In reality, the pathlength tends to slowly decrease with column density (because high column densities correspond to lines of sight reaching closer to the halo centers), but the effect is roughly cancelled by the increasing temperatures (Fig. 9c). The temperature increase is due to higher shock velocities in the denser regions. The flattening of both median temperature and neutral fraction at low column densities is an artifact of our algorithm for cloud identification, since there is a minimum neutral density, and therefore a minimum gas density and neutral fraction, for the gas inside clouds. This also gives a minimum temperature, since temperature correlates well with gas density.

The velocity divergence shows that most of the low column density systems are expanding near the Hubble rate. The gas in sheet-like and filamentary structures is typically expanding along them as it falls towards higher density halos; the infall rate of gas from surrounding voids declines, and

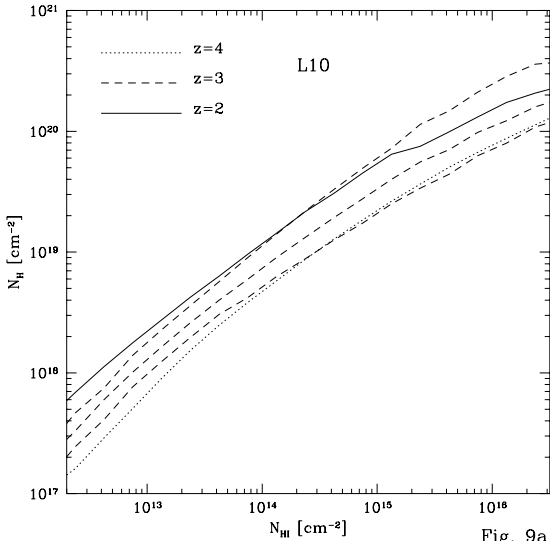


Fig. 9a

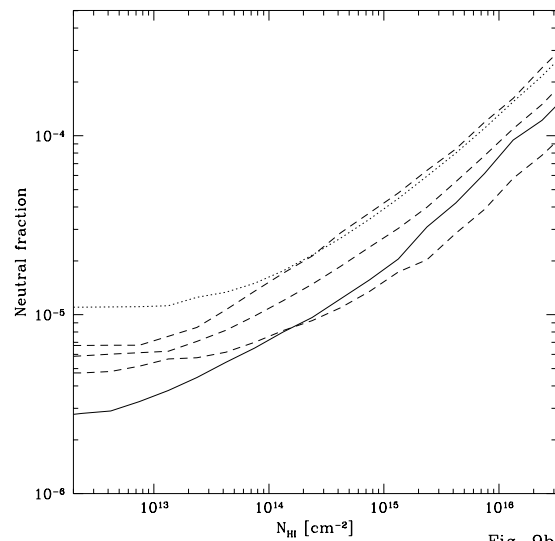


Fig. 9b

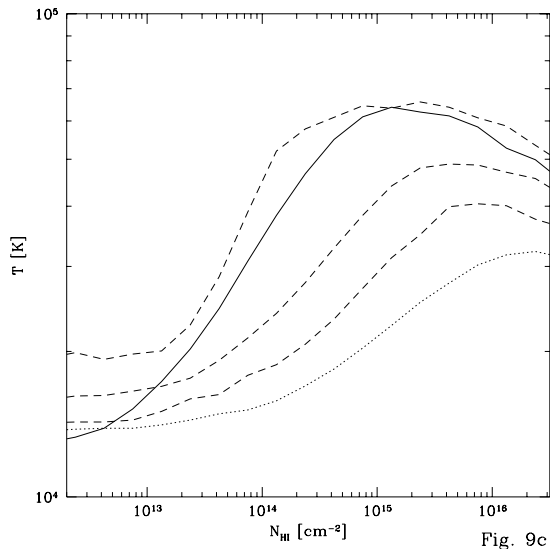


Fig. 9c

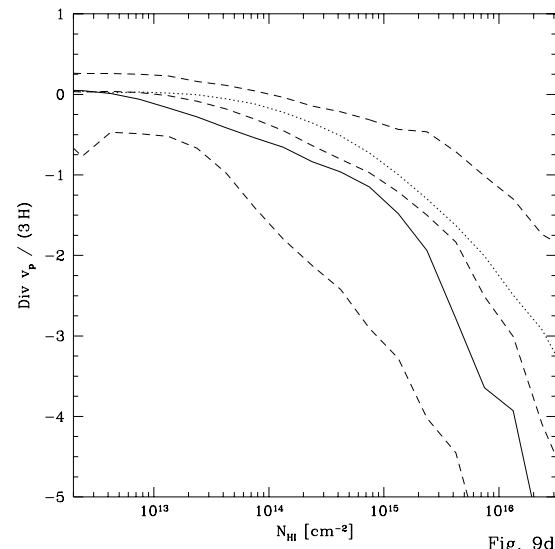


Fig. 9d

Fig. 9: (a) Thick lines give the median total column density at a fixed neutral column density, in the L10 simulation at three redshifts. The two thin dashed lines give the total column densities such that 5% of the clouds have a lower and higher column density. Both column densities are measured within a fixed contour of neutral density in real space. Other figures show the distribution of the neutral-weighted (b) neutral fraction, (c) temperature, and (d) velocity divergence, in the same way as Fig. 9a.

the dark matter density also decreases, so both the ram-pressure and gravitational confining forces decrease with time. The gas still contracts in comoving coordinates for ($N_{HI} \gtrsim 10^{13} \text{ cm}^{-2}$), and at higher column densities ($N_{HI} \gtrsim 10^{15} \text{ cm}^{-2}$) the gas is contracting in real space. These systems are associated with denser filaments and halos, where shocks occur frequently and the collapse can continue as gas cools radiatively. We have found that the curves in Figs. 9(b,c,d) change only

minimally when the total-hydrogen-weighted quantities are calculated.

4. ANALYSIS OF THE SIMULATED SPECTRA

In this Section we present quantitative predictions from our simulations for various statistical quantities that can be measured from the Ly α absorption spectra produced by the neutral gas. We first analyze the distribution and correlation function of the transmitted flux, and then present properties of absorption lines defined according to a new algorithm which is precisely defined and easy to implement. The results will be shown for the L10 simulation (on a $10h^{-1}$ Mpc box with 288^3 cells) at the redshifts $z = 2$, $z = 3$ and $z = 4$, which will indicate the expected redshift evolution (at lower redshifts, the effects of fluctuations on scales larger than the box size becomes more important). The results at $z = 3$ will be compared with the L3 and l3 simulations (on a $3h^{-1}$ Mpc box with 288^3 and 144^3 cells, respectively) to show the effects of the large-scale fluctuations and of the limited resolution. For each simulation at each redshift, the statistical quantities presented are computed from 18000 spectra corresponding to rows along one of the three axes in the simulation (these are selected from 1500 random groups of 12 parallel spectra at fixed distances, as described in §4.4).

4.1. Average Flux Decrement

The first statistical quantity that can be obtained from observed quasar spectra is the distribution of the transmitted flux. We start by considering the average transmission. This depends on our model for the ionizing background through the resulting intensity $J_{H\ I}$, and it therefore does not provide a strong test of the models. Instead, we must use the observed average transmission to fix $J_{H\ I}$, and then see if other predictions for the Ly α spectra agree with observations. Since our simulations were evolved for only one value of $J_{H\ I}$ (which, as mentioned in §3, is much too high to reproduce the observed flux decrement), and it is impractical to run many simulations with different $J_{H\ I}$, we must assume that varying $J_{H\ I}$ would only alter the neutral fraction in the gas, but the effects on the gas temperature and the consequent different dynamical evolution of the gas can be neglected. While it is reasonable that the small variation of the equilibrium temperature with $J_{H\ I}$ will not drastically change the results, this will have to be tested with more simulations in the future.

More generally, if we take the density, temperature and velocity fields of the gas in the simulations as constant and let the normalization of the gas density and the intensity of the ionizing background vary, then the density of neutrals changes proportionally to $(\Omega_b h^2)^2 / J_{H\ I}$ neglecting collisional ionization. The optical depth to Ly α scattering depends only on the column density of the gas, and therefore varies as $\mu^2 \equiv (\Omega_b h^2)^2 / (h J_{H\ I})$. Thus, we can approximate the variation in the predictions for the Ly α forest given by our simulations when we vary Ω_b and $J_{H\ I}$ by multiplying all the optical depths by the variation in the factor μ^2 , if we neglect collisional ionization, the self-gravity of the baryons, and the effects in the evolution of the gas due to the different cooling rate when the neutral fraction changes (notice that changing the Hubble constant would also imply a change in the power spectrum of our CDM+ Λ model).

As explained in §3, all our results on the simulated Ly α spectra will be presented assuming $J_{-21} = 0.1$, and $\Omega_b = 0.0355$ and $h = 0.65$ as used in the simulation. The neutral fractions have been

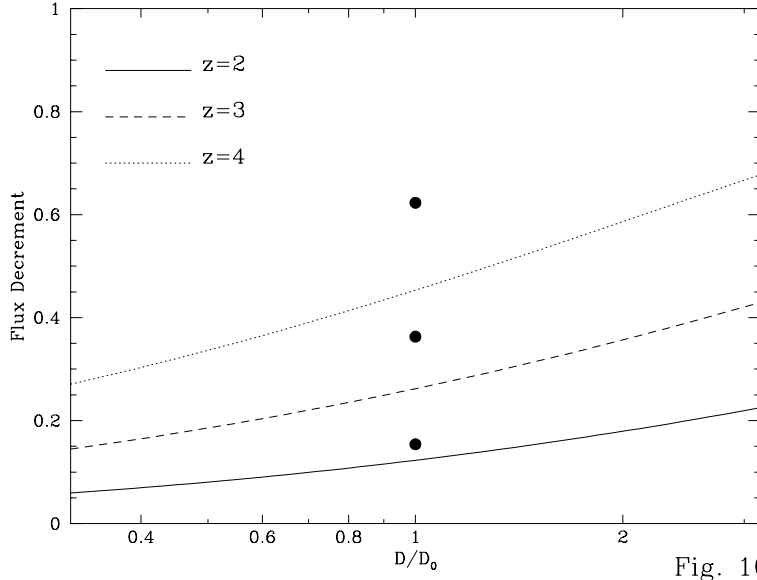


Fig. 10

Fig. 10: Average flux decrement in the Ly α spectra from the L10 simulation at $z = 2, 3$ and 4 , as a function of the factor D/D_0 by which the neutral densities are uniformly multiplied. We use $D/D_0 = 1$ in all subsequent figures, corresponding to the neutral fractions calculated assuming ionization equilibrium with a background intensity $J_{-21} = 0.1$, for $\Omega_b = 0.0355$ and $h = 0.65$, as in the simulation. The change with the factor D/D_0 is approximately the same as the change with Ω_b^2/J_{HI} , except for the effects of collisional ionization (which is negligible for the regions making most of the contribution to the average flux decrement), self-gravity of the baryons, and the change in the equilibrium temperature.

recalculated at every cell in the simulation for this value of J_{HI} , including both photoionization and collisional ionization. However, it is of interest to see how the predicted average flux decrement varies with the factor μ^2 , because the observational determination of the flux decrement is subject to some uncertainties due to the intrinsic noise in the observations, the extrapolation of the quasar continuum spectrum, and the contribution of metal lines and damped absorption lines (which our simulation does not include). For this purpose, we can assume that the optical depth varies proportionally to μ^2 , neglecting collisional ionization, because the regions where collisional ionization is important are always at high densities and they have a very large optical depth to Ly α absorption in any case.

The predicted flux decrement when the optical depths are multiplied by a factor μ^2/μ_0^2 is shown in Figure 10 (μ_0^2 is the value of μ^2 when J_{HI} and Ω_b have our standard values). The filled circles show the observed flux decrement determined in Press, Rybicki, & Schneider (1993). These observed values are still slightly higher than our results, but they include the contribution from metal lines and the damped wings of high column density systems. It is therefore not completely clear if the difference from the observations is real. A constant value of J_{HI} comes close to reproducing the observed evolution with redshift of the flux decrement; this is also similar to the dependence of $J_{HI}(z)$ obtained from our emission models (a precise fit to the values of Press et al. requires J_{HI} to increase by a factor ~ 1.5 from $z = 4$ to $z = 2$). Figure 10 can be used to see the amount by

TABLE 4: FLUX DECREMENTS

	L10, z=2	L10, z=3	L10, z=4	PRS
D_β/D_α	0.30	0.37	0.43	0.48 ± 0.05
D_γ/D_α	0.13	0.19	0.24	0.35 ± 0.07
D_δ/D_α	0.073	0.11	0.15	0.16 ± 0.08
D_ϵ/D_α	0.045	0.073	0.10	0.12 ± 0.07

which $J_{H\,I}$ or Ω_b need to be changed to fit any observed value for the average decrement. The value $\mu^2 = \mu_0^2$ is assumed throughout the rest of this paper.

We also give in Table 4 the ratios of the average flux decrements of all the Lyman series transition lines, up to Ly ϵ , to the Ly α average flux decrement, for the L10 simulation at three different redshifts ¹. These are calculated by simply multiplying the optical depths by the ratio of the oscillation strengths times the ratio of wavelengths of the Ly $(\beta, \gamma, \delta, \epsilon)$ lines to the Ly α line (equal to 0.16, 0.056, 0.027, and 0.015, respectively), and computing the average flux decrement. Determinations of these flux decrements were given by Press et al. (1993) (the average redshifts of their sample of Ly α absorption spectra is ~ 3.4). These are sensitive to the column density distribution: the more abundant the lines of high column density are relative to low column density, the higher a fraction of the Ly α decrement is contributed by heavily saturated lines, so the larger the decrements of the high order lines should be. As we can see, our predicted ratios of the decrements of high order Lyman lines to the Ly α decrement are smaller than observed, suggesting that the column density distribution we obtain is too steep. We shall return to that in §4.6.

4.2. Flux Distribution

The cumulative distribution of the transmitted flux in the spectra is shown in Figures 11(a,b). As seen in Figure 11a, the simulations with the smaller box yield more absorption. This is a consequence of the missing large-scale power in the small box simulation. One cause for the difference is the higher temperature, and the correspondingly lower recombination coefficient in the L10 simulation; the other is the fact that the distance separating successive lines is limited by the size of the box. The typical transmission in the Ly α spectra is mostly sensitive to the gas distribution in the voids, rather than the denser regions, since the voids occupy most of the volume in the universe. In the small box simulation, the size of the voids is limited and the separation between lines is smaller. The effect of the finite resolution is also to increase the average absorption, because the inclusion of collapse on small scales results in a lower gas density over most of the volume (more of the gas is concentrated in high-density, small-scale objects). The difference between the L3 and l3 simulations is, however, very small, because the scales that are unresolved are already below the Jeans mass of the photoionized gas. These results imply that *the effect of the finite resolution and size of the simulated box can only be to increase the amount of absorption that we obtain, so the true*

¹ We thank David Weinberg for suggesting to calculate these ratios

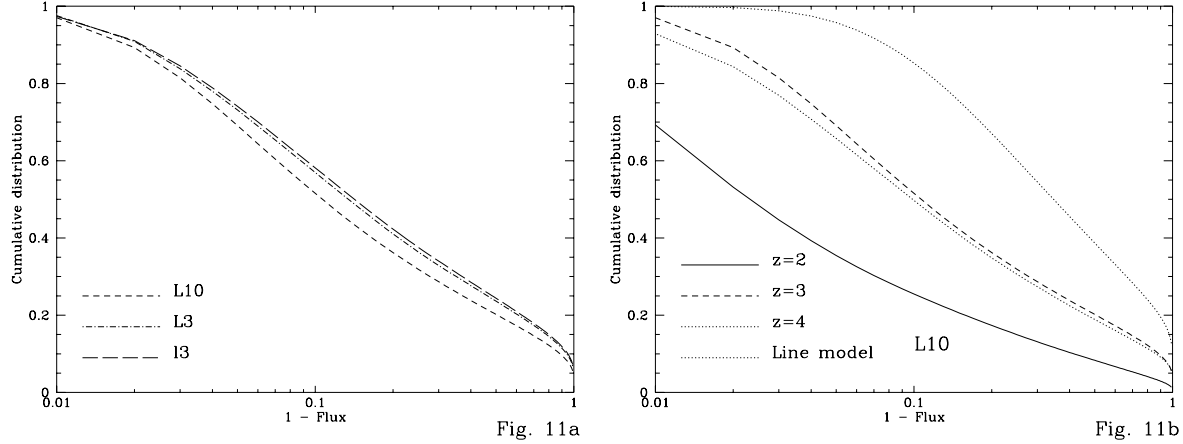


Fig. 11: Cumulative distribution of the absorbed flux (equal to one minus the transmitted flux), for the simulations and redshifts as indicated in the figure (line types for each simulation and redshift are the same in all figures). The thick dotted line in figure 10b is calculated from randomly generated spectra containing superposed lines with Voigt profiles with a distribution of column densities and b-parameters as described in §4.2, with the line density normalized to the observed one at $z = 3$, and it has a similar shape as the flux distribution from the simulations.

predicted absorption of the model should be lower than the results of the L10 simulation. Judging from the differences between the three simulations, the correct prediction is probably not lower by more than $\sim 10\%$ relative to L10. However, a possible effect that could increase the absorption found in our simulations is if the gas temperatures in the absorption lines were significantly lower due to additional cooling for the low value of J_{HI} we need to assume, which could also cause additional compression of the gas. This could be particularly significant if thin, cool slabs of gas between shocks were common and could not be resolved in our simulation.

The observations of the Ly α forest have customarily been reduced by decomposing the observed spectrum into a discrete number of absorption lines, assuming they are described by Voigt profiles (or gaussians for the optical depth, since the damped wings are not important for the low column density lines we are interested in). One then obtains distribution functions of the column density and b-parameters. In order to compare with observational results, we shall use a model for the distribution of N_{HI} and the b-parameters of the lines and then compute the distribution of the flux from artificially generated spectra, assuming that the lines are uncorrelated. Our model (which shall be called “line model” in our figures) has a column density distribution with $f(N_{HI}) dN_{HI} \propto N_{HI}^{-\beta}$, where $\beta = 1.5$ for $N_{HI} < 10^{14.8} \text{ cm}^{-2}$, and $\beta = 1.9$ for $N_{HI} > 10^{14.8} \text{ cm}^{-2}$. The total number of lines per unit redshift above $N_{HI} = 10^{14} \text{ cm}^{-2}$ is fixed to 100 at $z = 3$ (we shall only show results for this model at $z = 3$). The b-parameters are assumed to be uncorrelated to the column densities, and their distribution is chosen as a gaussian with the peak at $b = 27 \text{ km s}^{-1}$, a dispersion of 9 km s^{-1} , and a cutoff at $b = 17 \text{ km s}^{-1}$, so that no lines have b-parameters lower than the cutoff. This distribution is close to what is favored by the observations (e.g., Rauch et al. 1992; Petitjean et al. 1993, Hu et al. 1995), and as we shall see it provides a relatively good fit to the spectra obtained from our simulation.

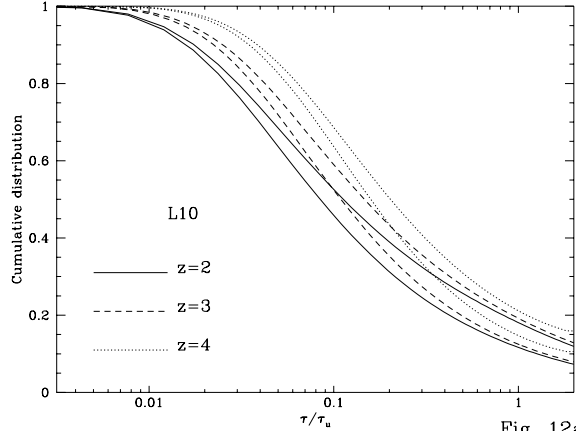


Fig. 12a

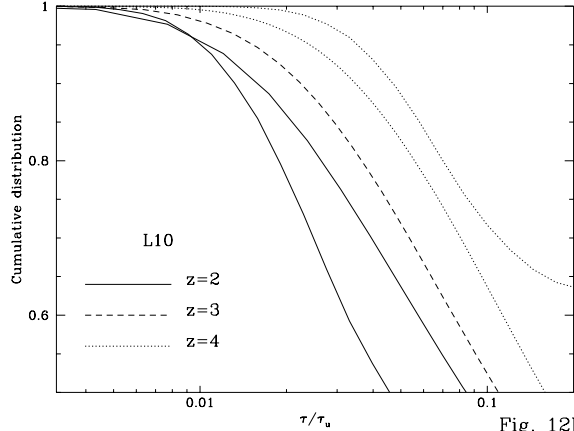


Fig. 12b

Fig. 12: (a) Thick lines are the same cumulative distribution as in Fig. 10, but as a function of τ/τ_u , where τ is the optical depth and τ_u is the uniform optical depth that would be observed for a uniform intergalactic medium of density Ω_b , and for the same intensity J_{HI} . The thin lines are the same cumulative distribution when thermal broadening is not included. (b) Thin lines are as in Fig. 11a, and thick lines are the analytical prediction from the “modified Zel’dovich approximation” in Reisenegger & Miralda-Escudé (1995).

The thick dotted line in Figure 11b shows the cumulative distribution implied by our line model, calculated from 1800 randomly generated spectra with the same velocity length as the L10 simulation at $z = 3$. Its shape is very similar to what is obtained from the L10 simulation, and the average decrement implied is 0.249, only slightly below the result of our simulation for $\mu^2/\mu_0^2 = 1$ (0.263). The shape of this distribution is a prediction of the CDMA model which should be directly testable with observations (see Jenkins & Ostriker 1991; Webb et al. 1992).

4.3. The Fluctuating Gunn-Peterson Effect

We see in Figure 11b that there is a fast evolution in the distribution of transmitted flux: the absorption increases rapidly with redshift. This is mostly due to the rapid increase of the optical depth that would be observed if the gas was uniformly distributed, $\tau_u = 4.65 \times 10^5 \Omega_{HI} h [H_0/H(z)]$ (Gunn & Peterson 1965; here, Ω_{HI} is the fraction of the critical density in neutral hydrogen in a uniform medium, H_0 is the present Hubble constant and $H(z)$ is the Hubble constant at redshift z). For the parameters of our simulation and $J_{-21} = 0.1$, this optical depth would be $\tau_u = 0.212$, 0.785 and 2.15 at $z = 2, 3$ and 4, respectively. Because the gas moves towards collapsed structures, leaving most of the volume with a density below the average, we expect that the optical depth over most of the spectrum is considerably below that derived for a uniform medium with the average density.

The cumulative distribution of the ratio τ/τ_u is shown in Figure 12a as thick curves for the simulation L10. This shows the true evolution that results from the gravitational evolution of the shape of the density field: as the redshift decreases, the gas continues to move away from the voids into collapsed objects, and the fraction of the spectrum with τ/τ_u below a fixed value increases. However, the evolution in τ/τ_u is quite small compared to the evolution seen in Figure 11b. Most of

the rapid increase of the typical absorption with redshift is due to the change in τ_u , which evolves as $(1+z)^{4.5}$ when $\Omega(z) = 1$ and J_{HI} is constant.

We also show as thin lines the distribution of τ/τ_u which is obtained if the thermal broadening due to the gas temperature is not included when the Ly α absorption spectra are computed. This removes the thermal wings of the absorption lines, and therefore increases the fraction of the spectrum with low optical depths. The difference from the thin to the thick lines is relatively small. In particular, we see in Figure 12a that most of the absorption in the regions with the lowest optical depths comes from a true fluctuating “Gunn-Peterson effect” arising from the most underdense regions of the intergalactic medium, rather than from thermal wings of the lines.

The distribution of τ/τ_u was calculated analytically by Reisenegger & Miralda-Escudé (1995), using an approximation they proposed, the “Modified Zel’dovich Approximation” (MZA). The CDMA model we have adopted in the simulations was also used by them, among various other models. In Figure 12b, we show again the thin curves of Figure 12a together with the MZA prediction given in Figure 4 of Reisenegger & Miralda-Escudé for $z = 2$ and 4 (plotted as thick curves; this is only shown in the region of validity of the MZA, for low optical depths). The agreement between the curves is probably better than could be expected given the approximations involved in the MZA (neglecting the gas pressure and assuming that the deformation tensor of any gas element conserves its shape), and given also the possible effects of the missing large-scale power in the simulation.

The distribution of the fluctuating Gunn-Peterson optical depth should be a sensitive probe to the amplitude of the primordial density fluctuations that are collapsing at the redshifts of observation. For high amplitudes, the voids should be much more empty and much lower optical depths should cover a large fraction of the spectra. The relatively good agreement of the numerical simulation and the analytical results of Reisenegger & Miralda-Escudé (1995) is also encouraging, since the predictions of different models can be anticipated approximately without the need for expensive computer simulations.

4.4. Correlation of Flux Along and Across the Line of Sight

We now take parallel rows along the simulation separated by a fixed number of cells. We define the correlation function of the flux as:

$$\xi_f(\Delta v, \Delta r) \equiv \left\langle \frac{(F_{\mathbf{r}}(v_0) - \langle F \rangle) - (F_{\mathbf{r}+\Delta\mathbf{r}}(v_0 + \Delta v) - \langle F \rangle)}{\langle F^2 \rangle - \langle F \rangle^2} \right\rangle, \quad (2)$$

where $F_{\mathbf{r}}(v)$ is the fraction of transmitted flux along a line of sight defined by a transverse vector \mathbf{r} , and v is the velocity along the spectrum. The average is done over the ensemble of all possible pairs of lines of sight.

The correlation function ξ_f is shown in Figure 13a for the L10 simulation at $z = 3$, as a function of Δv , at a number of different transverse separations Δr . To calculate the correlation, we have randomly selected 1500 groups of 12 rows from the simulation. We select one of the possible 3 axis of projection, and then one among 288^2 possible rows. Thus, the total number of choices is 248832 (since we did not avoid repeated choices, there is an average of 4.5 groups of 12 rows that appear twice in the sample). Within each group, the last 11 rows are separated from the first by the number of cells (and the proper separation Δr) indicated in Figure 13a. The correlation for $\Delta v = 0$ declines

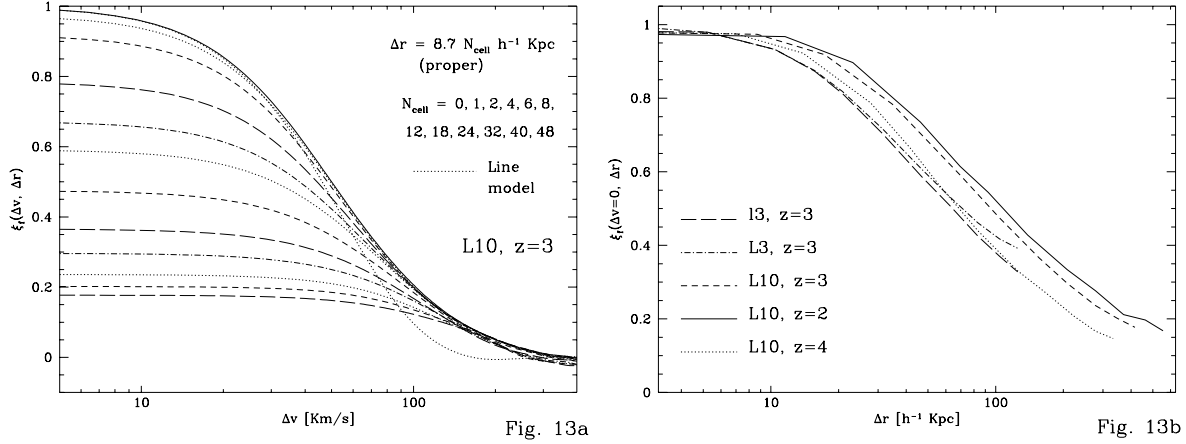


Fig. 13: (a) Solid line shows autocorrelation function of the transmitted flux as a function of velocity separation Δv in the spectrum, and other lines are the correlation function for spectra separated by a transverse distance Δr , as given in the Figure. Thick dotted line is the autocorrelation of the line model. (b) Flux correlation on parallel spectra as a function of transverse separation Δr , when $\Delta v = 0$.

monotonically with Δr , so the curve corresponding to each separation Δr is easily identified in the figure. The curve for $\Delta r = 0$ gives the autocorrelation function of the flux along a spectrum, and is plotted as a solid line. Also shown as a thick dotted line is the autocorrelation function of the flux for our line model described in §4.2 (we compute it from the same 1800 randomly generated spectra).

The autocorrelation for our line model agrees well with the simulation for $\Delta v < 30 \text{ km s}^{-1}$. For these low velocities, the flux autocorrelation depends mostly on the distribution function of b-parameters and column densities, and the agreement suggests that the spectra in our simulation should yield b-parameters similar to the observed ones (see also §4.8) if analyzed in the same way as the observations, since the b-parameters of our model are similar to the observed distribution (e.g., Rauch et al. 1992, Cristiani et al. 1995, Hu et al. 1995). An analysis of the simulated spectra using the same deblending techniques to fit lines as have been used in the observations will be done in a subsequent paper.

The flux correlation in our line model drops very fast for velocities larger than the maximum width of the lines. Our simulation results are clearly above the line model at $\Delta v > 50 \text{ km s}^{-1}$. This could indicate the presence of a correlation of the lines, or a tail in the distribution of b-parameters for high values above the gaussian in our model. The latter possibility, however, would also raise the correlation at low velocities. In any case, the flux autocorrelation is a directly observable quantity which our model predicts. In general, the distribution of b-parameters and the correlation function of the lines obtained from deblending techniques are quite sensitive to the detailed algorithm used to identify the lines.

The cross-correlation function can also be plotted for $\Delta v = 0$ as a function of Δr , the spacing of spectra perpendicular to the line of sight as measured by comparing absorption lines in quasars that appear close together on the sky. This is shown in Figure 13b. The correlation of the transmitted

flux is strong up to large transverse separations: it declines to 0.5 only at $80h^{-1}$ kpc, and there is still a significant correlation at $\sim 500h^{-1}$ kpc. The correlation simply arises because the absorption is produced by the large-scale structure of the universe; in particular, the filaments or sheets that cause the absorption (cf. Figure 2c) show extended linear structures. A simple “cloud” model as adopted by most previous investigators (usually considering spherical structures in dynamical equilibrium) would clearly predict a much smaller correlation on the large scales shown in Figure 13b. The absorption lines, as we can see directly in Figures 2 and 3, arise from intersection of the lines of sight with filaments and sheets, as well as clumps which might be approximated as “clouds”. We notice that the correlation tends to increase at lower redshift, but only by a modest amount. The smaller box simulation shows less correlation, owing to the missing large-scale power. There is practically no difference between the L3 and l3 simulations, since the structures are already well-resolved in the lower resolution simulation. The small difference shows that as the resolution is increased, the correlation on transverse scales also increases. This may at first sight seem paradoxical, since one might have intuitively expected that higher resolution should imply more small-scale variations of the density, and therefore a loss of the correlation on large scales. However, the structures causing the absorption are caustics where the gas is shocked, which are intrinsically smooth due to the erasure of small-scale power that the gas pressure causes on the gas density field. The absorbing structures in the high-resolution simulation are equally smooth, and the better correlation is due to a decrease in the numerical noise arising from the finite number of cells across the absorbing clouds.

Our model is probably in agreement with recent observations of line correlations (see Smette et al. 1992, 1995 Bechtold et al. 1994, Dinshaw et al. 1994, 1995), although that will have to be tested by line identification using the same procedure as in the observations. We must also caution about the fact that the observed line correlation has been found for strong lines, whereas our flux correlation is sensitive to weaker lines. If the spectra of a quasar pair can be observed with high signal-to-noise, then the analysis of the flux correlation can also be compared with our prediction. We notice that the correlation on parallel lines of sight remains appreciable over a substantial range of Δv (see Figure 13a), and that one should not just search for “line coincidences”, but use also the information which is in the flux fluctuations in the spectra which do not correspond to significantly detected lines.

4.5. Number of Lines

The statistical information contained in the spectra of the Ly α forest is entirely contained in all the N-point correlation functions of the flux. In fact, if the spectra were one-dimensional gaussian fields, as could be the case if the collapsing structures producing the absorption were still in the linear regime, then the one-point correlation function would already provide all the information and all higher order correlations could be derived from this. In practice, the absorbers are already at an advanced nonlinear stage of the collapse and the spectra are highly non-gaussian, so that statistical measures other than the higher order correlation functions may be more useful in comparing observations with theoretical predictions. One of the characteristics of the Ly α forest is the presence of discrete absorbers, which correspond to individual collapsing objects in our simulations. However, the shape of the absorption profiles is determined by the distribution of hydrodynamic velocities within the system in addition to the gas temperature, and therefore the total velocity distribution is generally non-gaussian. If the shape of an absorption profile is “deblended”

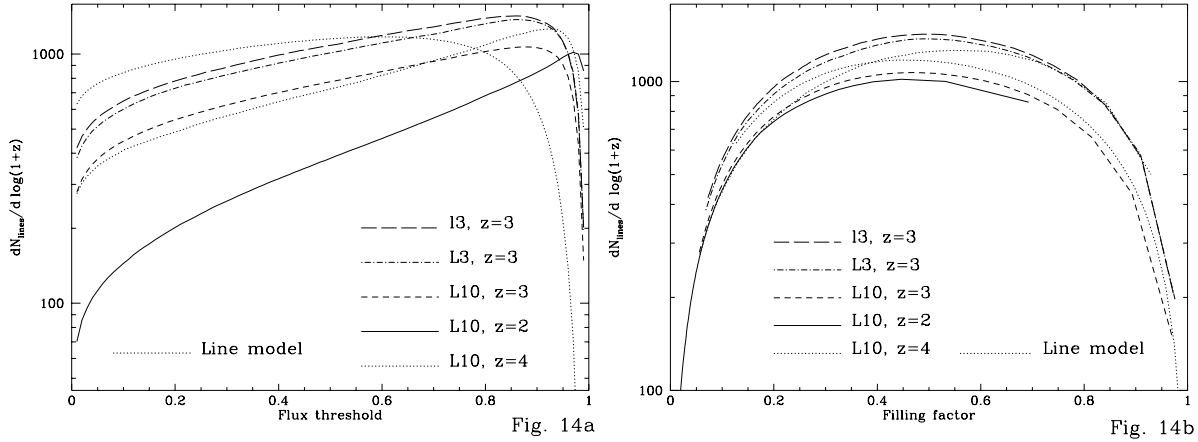


Fig. 14: (a) Number of lines per unit $\log(1+z)$, as a function of flux threshold F_t , where a line is any region of a spectrum where the flux is $F < F_t$ continuously. (b) Same number of lines is shown as a function of the filling factor in the spectra of the regions with $F < F_t$.

into several Voigt profiles to obtain a fit, the separate profiles do not necessarily correspond to individual physical components, and the fitted b-parameters and column densities are not necessarily related to physical quantities. On the other hand, when two such lines are only partially “blended”, but they still show two clear minima in the transmitted flux, they often correspond to separate physical systems.

Thus, a measure of the number of lines should give another useful statistical quantity. The detection procedure to identify lines should be performed using a well defined algorithm which is simple to implement, but its relation to fitted Voigt profiles is less important. Such a detection is straightforward in low redshift, low signal-to-noise spectra, where the flux fluctuations are dominated by noise over most of the spectrum and the detected lines are well separated (e.g., Schneider et al. 1993): one simply imposes a minimum equivalent width to any detected lines. But here we are interested in the regime where the true fluctuating continuum of absorption is observed and any identified “lines” are blended among them and with this continuum (notice that in the theory of gravitational collapse we are simulating, a true fluctuating continuum is present also at low redshift, although a much higher signal-to-noise is required to observe it). Here, we propose an algorithm based on the same concept of a cloud introduced in §3 in real space, which was also presented and used in HKWM. For any given flux threshold F_t , we identify all the regions where the flux is below this value and call them “lines” (the flux threshold plays an equivalent role to the contour of neutral density in real space). All the lines are therefore bounded by two points in the spectra where $F = F_t$. As an example, Table 5 (in §4.7) gives the lines identified in the spectra plotted in Figures 7(a,b,c,d) and 8(a,b), when $F_t = 0.7$. The first column shows the central velocity of the lines, and the other two columns give the column densities and b-parameters measured as explained below (§4.6 and 4.7). Many fewer lines are detected compared to the deblending method, since the lines in Table 3 are blended and the weakest ones do not reach below the threshold F_t . To apply this algorithm to observational data, one should probably impose the additional requirement of a minimum equivalent width.

We start discussing the number of such lines in the simulated spectra. Figure 14a shows the number of lines per unit $\log(1+z)$ detected according to this algorithm. Each curve was computed from the same 18000 spectra described in §4.4, and the curve for our line model was computed from 1800 random spectra. The number of lines is shown as a function of the flux threshold. Strong lines are counted for low flux threshold, since the optical depth has to reach a lower minimum in the line profile. The number of lines increases as the flux threshold is raised, and it starts decreasing at some point due to blending when the lines start covering most of the spectrum. The same number of lines is shown in Figure 14b as a function of the filling factor, defined as the fraction of the spectrum occupied by the regions with $F < F_t$, identified as lines. The filling factor was shown as a function of the flux threshold in Figures 11(a,b). Again, low filling factor corresponds to strong lines.

We notice that the curves shown in Figures 14b are totally independent of the factor μ^2 by which we may multiply the optical depth in order to vary the average flux decrement. Thus, the number of lines as a function of the filling factor is a completely new piece of information once we have fixed the average flux decrement, in contrast to the number of lines above a fixed column density. These curves are an independent testable prediction of our model, related to the scale of the fluctuations in the absorption.

As before, we see that the difference between the l3 and L3 simulations is extremely small, and that the L10 simulation has $\sim 25\%$ fewer lines. Again, this is due to the large-scale power which is absent in the small box simulations. The L10 simulation has larger voids, and these result in long voids in the spectrum. The Jeans length of the gas is larger in a large-scale void, so the dark matter fluctuations within voids will often not affect the gas, and no lines will be produced.

We also see in Figure 14b that there is very little change in the number of lines with redshift. Our simulations predict that *when the number of absorption lines is measured at a fixed filling factor, there is practically no evolution with redshift*. Neither merging of structure, nor fragmentation, nor appearance of new structures is a major effect over the redshift interval considered. Most of the observed evolution is due to the increase in the mean opacity of the universe τ_u as expressed in classical Gunn-Peterson calculations. The small evolution seen in Figure 14b is probably due to the larger scales collapsing at $z = 2$, compared to $z = 4$: there is more spacing between successive structures, and the voids grow bigger and more underdense at low redshift (see also Fig. 12a). We emphasize that since the curves in Figure 14b are independent of the parameter μ^2 , the predicted evolution of the Ly α forest in this plot is independent of the value of J_{HI} and Ω_b , and is therefore a genuine prediction of the simulation. Of course the evolution at a fixed filling factor is more difficult to determine observationally, because very high signal-to-noise is required at low redshift for high filling factor, and at high redshift for low filling factor.

The evolution of the Ly α forest has been measured for lines above a fixed column density, or equivalent width, and it has been found that the number of lines per unit $\log(1+z)$ increases rapidly with redshift in this case, proportionally to $(1+z)^{\gamma+1}$, where $\gamma \simeq 2.5$ (e.g., Lu, Wolfe, & Turnshek 1991). Our results say that this evolution is mostly due to a general increase of the optical depth, evolving similarly to the Gunn-Peterson optical depth: $\tau \propto (1+z)^6 H^{-1}(z) \Omega_b^2 / J_{-21}$ (see also HKWM). The evolution in the “shape” of the Ly α forest is what is shown in Figure 14b and is very weak; the observed evolution is of the “amplitude” of the Ly α forest. For constant J_{HI} and temperature, the optical depth will increase as $(1+z)^{4.5}$ (notice that in our model, $\Omega(z)$ is practically equal to one at $z > 2$), and if the gas in the Ly α forest is expanding at the Hubble

rate this will cause an evolution of the number of lines above a fixed column density proportional to $(1+z)^{4.5(\beta-1)}$, similar to the observed evolution for $\beta = 1.75$. In reality, the overdensities of the absorbing gas tend to increase (especially for high column density systems; Fig. 9d), but the increasing temperatures at low redshift compensate for that.

Finally, we compare our result for the L10 simulation at $z = 3$ with our line model. Figure 14b shows that the line model has an excess of lines at high covering factor, by about 25%. We might want to solve this by making the column density distribution shallower at low column densities; however, this would also change the distribution of flux at very low optical depths. We see from Figure 11b that the fraction of spectrum having very low optical depths is already substantially higher for our line model than in the simulations. If the number of weak lines is reduced, this fraction will be further increased. Thus, a model with superposed Voigt profiles with uncorrelated positions and similar b-parameters for weak and strong lines cannot reproduce both the flux distribution and the number of lines as a function of the covering factor. This is a sign of the presence of the Gunn-Peterson effect, produced in our simulation by gas in the voids that fills the volume between the structures yielding the absorption lines. This Gunn-Peterson optical depth fluctuates owing to the density variations across the voids, but it is a smoother variation than that caused by superposed weak lines; in particular, it has many less minima in the transmitted flux, hence the lower number of lines at high covering factor.

4.6. The Column Density Distribution

We now take the individual lines detected according to the prescription specified above, and integrate the optical depth over the interval in the spectrum between the two points where the flux is below our threshold F_t . The column density within this interval is then given by $N_{HI} = (m_e c) / (\pi e^2 f \lambda) \int dv \tau = [7.445 \times 10^{11} \text{ cm}^{-2} (\text{km s}^{-1})^{-1}] \int dv \tau$ (Gunn & Peterson 1965; here, $f = 0.416$ is the oscillator strength, and λ the wavelength of the Ly α line). Notice that the optical depth contributed by any element of gas in a physical system will be only partially included in the total column density of a line defined in this way, since the optical depth from the gaussian tails of the thermal velocity distribution will fall outside the interval corresponding to the absorption line. As the flux threshold is raised, the column density of each line will increase as the tails in the profile are included, and as it merges with its neighbors.

The distribution of column densities found in this way is shown in Figure 15a as the thick lines, for the L10 simulation at $z=3$, for four different flux thresholds corresponding to the filling factors indicated in the figure. Also shown as thin lines are the column density distribution obtained in the same way for our line model. Finally the thin solid line is the true distribution of column densities assumed in our line model. There is generally good agreement among the curves obtained from the simulations and those of the line model. For $N_{HI} > 10^{15} \text{ cm}^{-2}$, the agreement of the solid line with the other thin lines show that these column densities are, as expected, appropriately recovered from our algorithm. At the same time, the fact that for low column densities the column density distribution of the line model obtained from our algorithm agrees well with the results from the simulation shows that the turnover in the column density distribution at low column densities is partly due to our algorithm. This is also as expected: some lines are entirely missed when their flux minimum is above the threshold, and the detected lines also lose the column density in the tails of their profiles that are above the threshold. Since the line model agrees well with the determinations

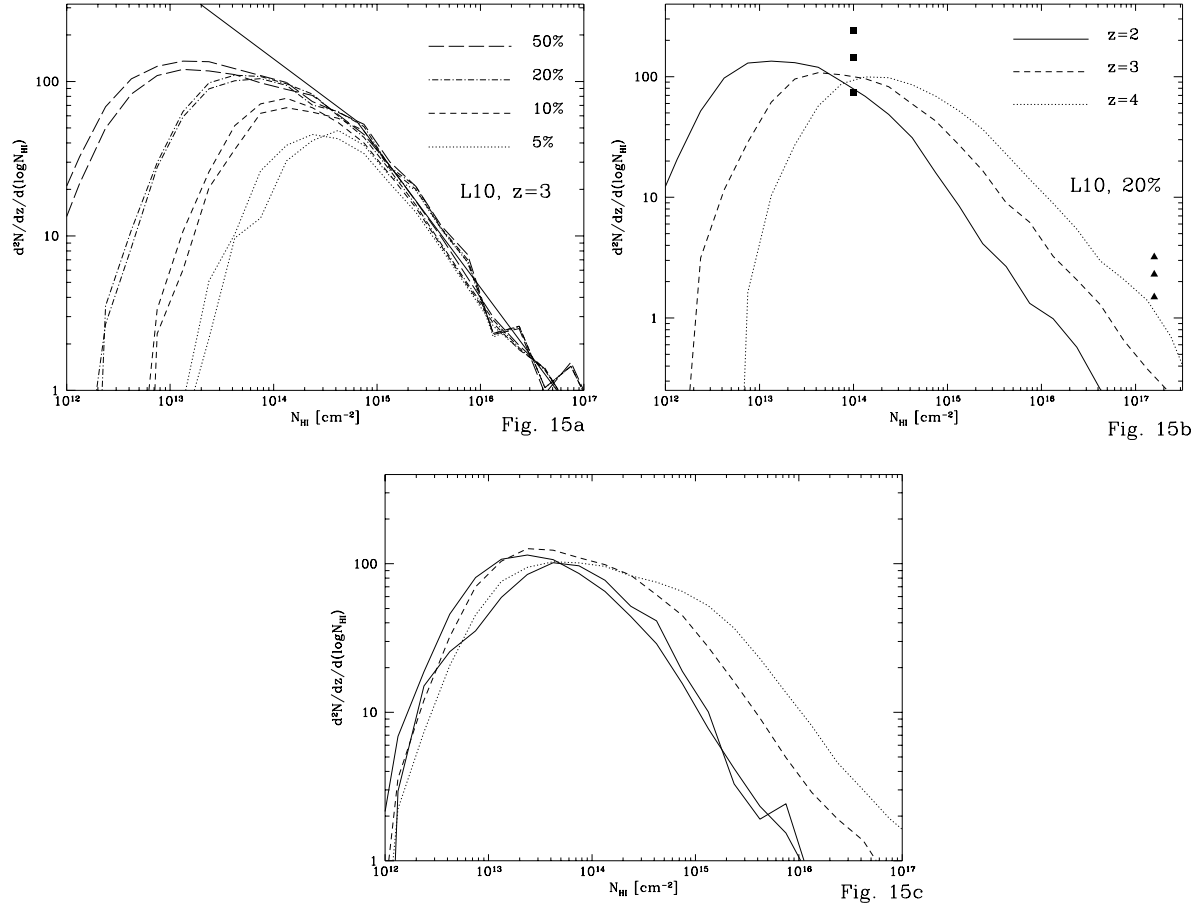


Fig. 15: (a) Thick lines are column density distribution at $z = 3$ in the L10 simulation for filling factors 10%, 20% and 50% (corresponding to flux thresholds $F_t = 0.107, 0.486$ and 0.891 , respectively). Results for line model are shown as thin lines, thin solid line is the true column density distribution of line model. (b) Column density distribution for filling factor of 20%, at $z = 2, 3$ and 4. Black squares are observed number of lines at $z = 3$ $N_{\text{HI}} = 10^{14} \text{ cm}^{-2}$ from Petitjean et al. (1993), and assuming evolution as $(1+z)^2 \cdot 3$ for $z = 2$ and $z = 4$. Black triangles are number of Lyman limit systems at $z = 2, 3$ and 4 from Stengler-Larrea et al. (1995; we assume a slope $\beta = 1.5$ of the column density distribution to transform their cumulative number of Lyman limit systems to a differential number). (c) Column density distribution at a fixed flux threshold, $F_t = 0.7$. The thick solid line is the distribution obtained by HKWM (using an SPH simulation and for a CDM model different from the one we adopt).

of the column density obtained using the deblending technique (Petitjean et al. 1993; Hu et al. 1995), it seems probable that our simulations should also yield results in agreement with observations when analyzed in the same way.

We also show in Figure 15b the column density distribution from the L10 simulation at $z = 2, 3$ and 4, fixing the filling factor to 20%. The black dots indicate the observed number of lines at $N_{\text{HI}} = 10^{14} \text{ cm}^{-2}$, taken from Petitjean et al. (1993) at $z = 3$, and assuming evolution with

$\gamma = 2.3$ for the other two redshifts. The evolution at a fixed column density probably agrees with observations, once the effect of our algorithm shown in Figure 15a is taken into account. Since we have assumed a constant intensity of the ionizing radiation, the result suggests that if our simulation provides a correct description of the Ly α forest J_{HI} does not vary by a large factor within this redshift range, which is corroborated by the sources of ionizing photons that can be expected and the effect of the absorption by the Ly α clouds (see Table 2, and Cen & Ostriker 1992). The predictions for Lyman limit systems ($N_{HI} \sim 10^{17} \text{ cm}^{-2}$) are, on the other hand, clearly discrepant with observations. The observed number of Lyman limit systems at $z = 2, 3, 4$ is shown as solid triangles (Sargent, Steidel, & Boksenberg 1989; Storrie-Lombardi et al. 1995; Stengler-Larrea et al. 1995). Not only we have too few of them in the simulation (by a factor 10 at $z = 3$), but also they evolve much faster than is observed. A deficit of Lyman limit systems was also found in Katz et al. (1995); it may indicate the presence of a second population of absorbers at high column densities which are not reproduced in the numerical simulations, and the self-shielding effects which we have not included.

Finally, in Figure 15c we show the column density distribution at a fixed flux threshold $F_t = 0.7$, and we compare with the results at $z = 2$ for the CDM model in HKWM (*thick solid line*). Interestingly, the number of lines at high column densities is very similar (with a slight excess in the HKWM simulation) even though the two simulations are of two different theories. This suggests that the column density distribution is not a very sensitive test of the model, once they are all normalized to the same average flux decrement (the HKWM results were actually normalized to a slightly larger flux decrement). The smaller number of weak lines in the HKWM results may arise from their lower mass resolution, since weak lines tend to be produced by the small-scale systems that survive in large-scale voids, but it could also be a real difference of the models.

4.7. Other Properties of the Absorption Lines

We now measure equivalent widths and b-parameters of the absorption lines, using also the same procedure as in HKWM. In this paper, we shall only highlight the main results; a complete analysis of properties of individual absorption lines will be presented in a future paper, where various methods for measuring such properties will be tested and applied to observations and to the simulated spectra in the same manner. The results for this Section are obtained from an independent set of 3600 random spectra of the L10 simulation at $z = 3$. Equivalent widths of absorption lines are easily measured when lines are well separated in the spectrum. However, when lines are blended the equivalent widths are no longer well defined and depend on the “deblending” algorithm. In particular, if lines are fitted to Voigt profiles, the number of components required will increase with the signal-to-noise of the observation, and therefore the equivalent widths of individual components will on average decrease with the signal-to-noise.

We therefore use a different definition of the equivalent width, depending on the flux threshold used to select lines as described in §4.5. The equivalent width is measured only within the region where the flux is below the threshold, without attempting to add any tails of the absorption profile outside this region and without deblending. It is defined as the integral of $1 - F$ over the region between the two crossing points where $F = F_t$ (F is the transmitted flux). We show as thick lines in Figure 16a the distribution of equivalent widths, for three different flux thresholds; also shown, as thin lines, is the distribution obtained from our line model defined in §4.2. The thick dotted line

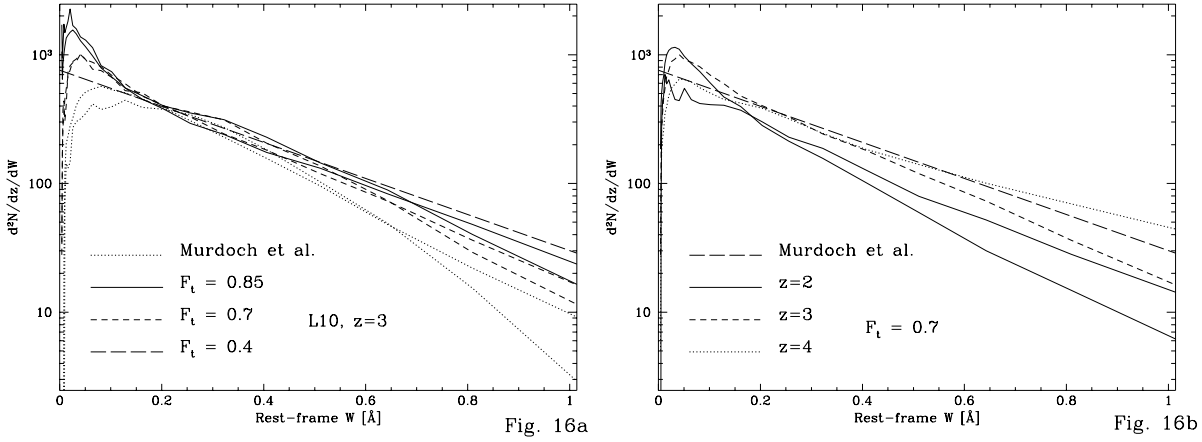


Fig. 16: (a) Thick lines show the equivalent width distribution at $z = 3$ from the L10 simulation, at three different flux thresholds. Thin lines are the same distribution obtained from the line model. The long dashed line is the exponential distribution in Murdoch et al. (1986). (b) Same distribution for the L10 simulation at $z = 2, 3, 4$, for $F_t = 0.7$. The thick solid line is the equivalent width distribution obtained by HKWM at $z = 2$.

is the exponential fit to the observed distribution given by Murdoch et al. (1986). The resulting distribution depends sensitively on the adopted flux threshold: it steepens as the flux threshold is lowered, because the large equivalent widths lines are split. This dependence on the flux threshold is well reproduced by our line model. An exponential profile provides a good fit to the equivalent width distribution we obtain, and the slope is similar to the observed one for $F_t = 0.85$. The excess of weak lines at low equivalent widths above the exponential fit is also present in the observed Ly α spectra (Murdoch et al. 1986; Hu et al. 1995), and agrees well with what is obtained for the line model, which incorporates weak lines with a power-law distribution of column densities with $\beta = 1.5$.

Shown in Figure 16b are the same equivalent width distributions for $F_t = 0.7$ at three different redshifts, and the equivalent width distribution found in HKWM at $z = 2$. We see again that our simulation contains more weak lines than HKWM. At high equivalent widths, the slope is slightly different. This results partly from the larger b-parameters (as we shall see below), and partly from the higher average flux decrement of the model of HKWM, since for a higher flux decrement a fixed flux threshold will correspond to a larger covering factor, which increases line blending and the number of high equivalent width systems.

The b-parameters of the lines are defined as being the same as that of a Voigt profile that has the same width of the interval where $F < F_t$, and the same equivalent width measured as above (i.e., not including the tails of the line profile where $F > F_t$). Figure 17a gives the distribution of b-parameters as a function of column density, measured as in §4.6. The five solid lines plotted indicate the value of b such that (5%, 25%, 50%, 75%, 95%) of the lines have a lower b-parameter at each column density. The dotted lines are the same results predicted by our line model. Most of the $b - N_{HI}$ correlation seen in the figure is caused by our algorithm to measure b , as seen from the curves for the line model (there is no intrinsic $b - N_{HI}$ correlation in the assumed line model). However, for $N_{HI} > 10^{14} \text{ cm}^{-2}$, some of the increase of b with N_{HI} seems to be real. This is probably

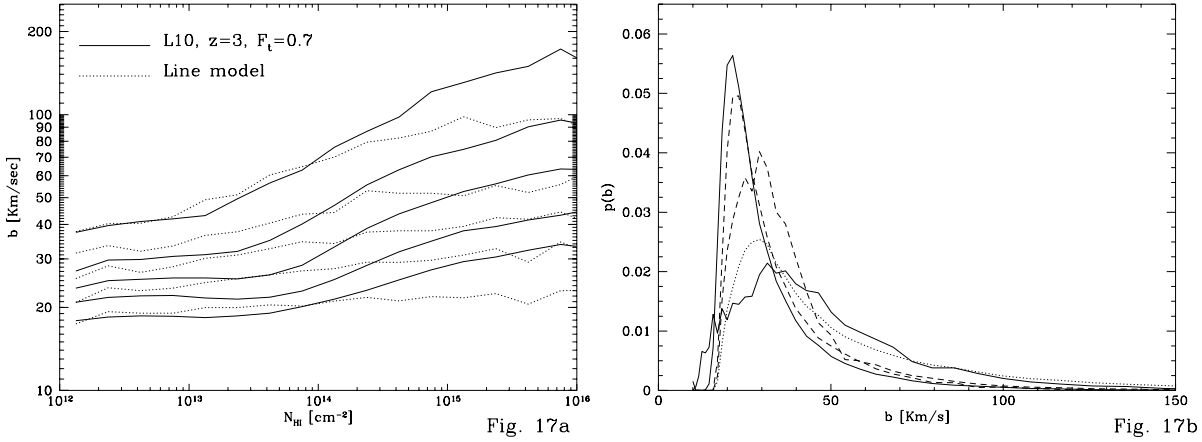


Fig. 17: (a) Distribution of b-parameters of lines found with a flux threshold $F_t = 0.7$. At each column density, the five solid curves show where (5%, 25%, 50%, 75%, and 95%) of the absorption lines have lower b-parameters. Dotted lines are computed for the line model. (b) Distribution of b-parameters for all lines, detected with $F_t = 0.7$. Thin lines show results from L10 simulation, thick solid line is the result from HKWM, and thick dashed line is the result for our line model.

due to the presence of hot gas in the dense regions of the high column density systems, caused by high velocity shocks, and also by cool gas falling at high velocity towards the system. Deblending techniques may not be able to recover such a correlation, since the dense cool gas in the system will cause a narrow minimum of the line profile, and the outer tails may be fitted with other weak lines; this would cause a correlation of the weak lines with the strong lines. The typical b-parameters obtained from the simulation and the line model also agree well, suggesting therefore that they also agree with the observations.

We also show in Figure 17b the probability density of the b-parameter for all lines detected at a threshold $F_t = 0.7$, at three redshifts, and compare the result at $z = 2$ with the same distribution obtained by HKWM. The b-parameters are remarkably different in the two simulations. Our b-parameters are smaller and have a smaller dispersion than in HKWM, and they show a very pronounced lower cutoff at $b = 17 \text{ km s}^{-1}$. The mean value we find at $z = 2$ is $\bar{b} = 33 \text{ km s}^{-1}$, compared to $\bar{b} = 50 \text{ km s}^{-1}$ in HKWM. The average flux decrement in HKWM was higher, and this can contribute to the larger Doppler parameters they find. However, raising the flux threshold to $F_t = 0.85$ (roughly equivalent to increasing the optical depths by a factor of 2, which is what is needed to bring our flux decrement to the value adopted by HKWM; see Fig. 10), our mean b increases only to $\bar{b} = 36 \text{ km s}^{-1}$. Thus, there is a genuine difference between the b-parameters, which could be due to a difference in the models or in the numerical methods of the simulations (in particular, the lower mass resolution in HKWM may cause some narrow lines from low-mass systems to be missed).

In Table 5, we give the b-parameters and column densities measured with the threshold method for the lines identified in the six spectra in Figs. 7 and 8. Many fewer lines are identified compared to the deblending method (see Table 3). The number of lines in Table 3 is particularly large because the signal-to-noise assumed was very high, so many lines are required to fit in detail the absorption

TABLE 5: ABSORPTION LINE PARAMETERS

v [km/s]	<i>b</i>	$\log N_{HI}$
	Fig. 7a	(z = 3)
112.5	30.9	14.86
600.0	84.8	14.43
936.0	96.4	15.16
	Fig. 7b	(z = 3)
328.7	74.8	15.52
1056.3	40.4	13.70
1143.9	21.3	13.59
	Fig. 7c	(z = 3)
93.8	23.4	14.17
259.0	49.6	14.94
764.5	26.4	13.68
987.2	37.9	13.39
1094.5	36.6	14.58
	Fig. 7d	(z = 3)
71.7	40.9	15.35
249.1	29.8	13.92
998.1	23.3	14.24
1182.4	31.4	14.29
	Fig. 8a	(z = 2)
99.2	23.9	14.12
422.8	27.4	13.24
727.3	24.7	13.38
928.0	40.1	14.22
	Fig. 8b	(z = 4)
105.4	109.2	15.46
382.8	41.1	13.90
895.4	176.1	15.85

profiles. The values of the parameters agree only for isolated lines. If the column densities of the blended lines are added together, they are generally larger than the column densities in Table 5. The reason is that high column density systems tend to have their profiles fitted with superposed lines of lower column density, and a central highly saturated line with a low *b*-parameter, and an

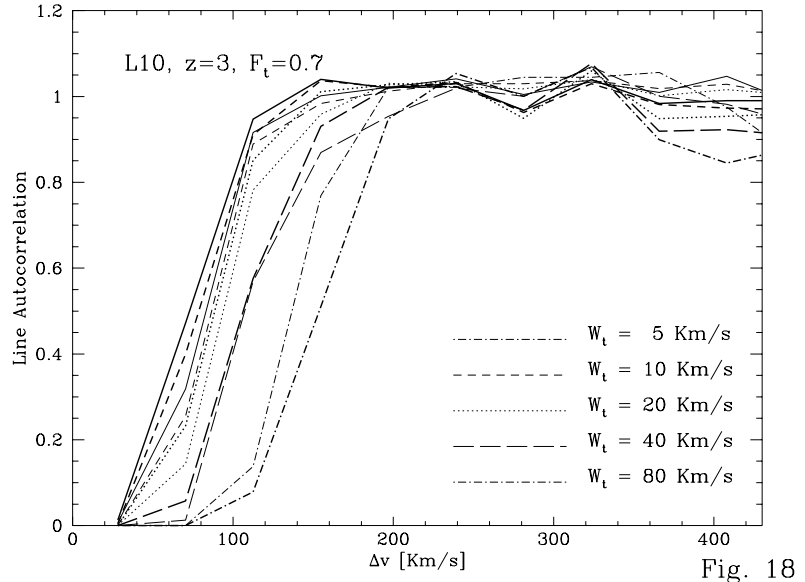


Fig. 18

Fig. 18: The autocorrelation function of lines along a spectrum, for all lines detected with $F_t = 0.7$ with equivalent width higher than the specified threshold W_t . Thick lines are for the L10 simulation, thin lines are for our line model. The anticorrelation at small separations is due to the width of the lines.

overestimated column density. This is highly sensitive to the assumed signal-to-noise, but it shows that the parameters derived from deblending of complex profiles are not necessarily related to the physical properties.

4.8. Correlation of Lines Along and Across the Line of Sight

The observations of correlations in the Ly α forest have most often been done from line identifications. In general, the correlation that is found will depend on the algorithm used to identify lines. In the usual deblending algorithm, the correlation of the lines will depend on the signal-to-noise of the observation. At low signal-to-noise, many absorption features will be fitted adequately with only one Voigt profile, and a negative autocorrelation will be found for separations of the order of the thickness of the lines. But at high signal-to-noise, several superposed Voigt profiles may be required to fit the shapes of the lines, and the correlation on small scales will be increased. In fact, the line detection algorithm affects the measured correlation on arbitrarily large velocity separations, because it can change the density of lines in a way which is not necessarily linear.

Here, we shall present the velocity correlation function of lines along the line of sight selected with the algorithm we have proposed, but we emphasize that this cannot be directly compared with the correlation of lines in the observations identified with other methods. We show the line autocorrelation in Figure 18 (the number of lines at a separation Δv from another line, divided by the expected number given the line density), where the lines are identified using the fixed flux threshold $F_t = 0.7$, and in addition we require the equivalent width (defined as in §4.7) to be above a

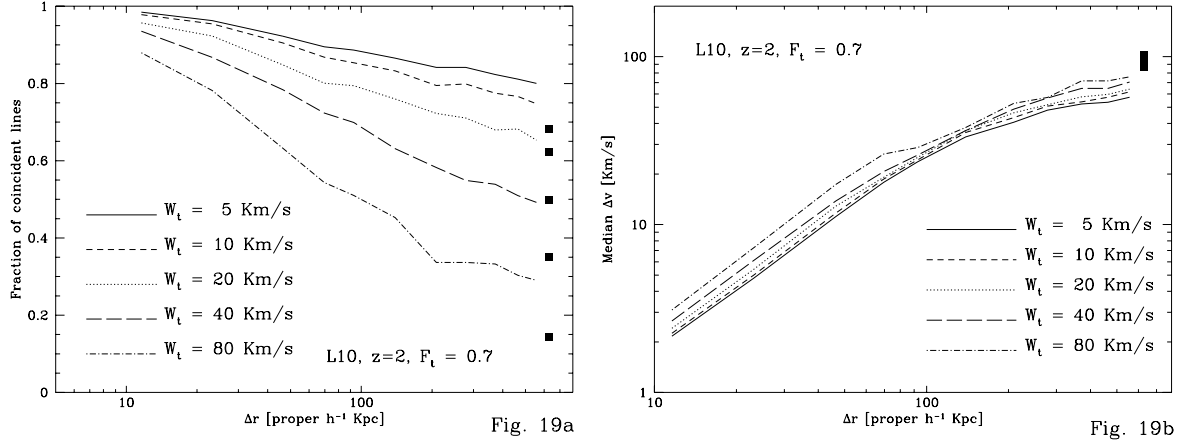


Fig. 19: (a) Fraction of lines in a spectrum above the equivalent width threshold W_t which have a coincident line in the spectrum from a parallel row at transverse distance Δr , also with $W > W_t$, with a central velocity differing by less than 1/4 of the box size (281 km s^{-1}). Black squares indicate fraction of coincident lines if they are placed randomly. Results are shown at $z=2$ to reduce the number of chance coincidences. (b) Median of the velocity separation Δv between coincident lines. Black squares indicate the median of randomly placed lines; these were computed by taking random pairs of rows from the simulation and shifting them in velocity.

given threshold W_t . The five curves are for five different thresholds in equivalent width, as indicated in the figure. The thick lines are the results from the L10 simulation at $z = 3$, and the thin lines are obtained from the line model described in §4.2 (in which there is no intrinsic spatial correlation). The thin and thick lines are quite similar, indicating that the anticorrelation at small velocities is entirely due to our algorithm for defining lines. The only difference with the line model appears to be that the simulation shows a larger spread of the Δv where the autocorrelation has a fixed value, as W_t is varied. This may be caused by a correlation of weak lines with the strong lines (which is expected from the infalling gas and shock-heated gas in the Ly α absorbing systems, as described in §3.3), which would increase the “zone of avoidance” around every strong line where other strong lines cannot be found. However, the effect is small, and the similarity of the curves with the line model emphasizes the importance of working directly with the flux correlation function. Unfortunately, we cannot investigate the correlations on large scales due to the small size of the box.

Next, we compute the fraction of coincident lines above a given equivalent width threshold on parallel lines of sight (i.e., the fraction of the time that a line with $W > W_t$ is detected on one line of sight when another line with $W > W_t$ has been detected on a parallel line of sight at a transverse distance Δr). This is shown in Figure 19a, again using $F_t = 0.7$ for line detection, and at $z = 2$. In addition to the equivalent width thresholds, we require that the lines are separated in velocity by less than 1/4 of the box size (281 km s^{-1}). We choose here the lower redshift because lines are much more crowded at higher redshift (increasing the fraction of chance coincidences), and because the observations have been done at low redshift. The black squares on the right show the number of chance line coincidences expected (obtained by computing the number of coincident lines with any two random rows of the simulation, and shifting one of two spectra by a random velocity). Most

of the lines are coincident on small scales, and the coincidences are reduced to about half the lines (when chance coincidences are subtracted) on scales $\sim 100h^{-1}$ kpc. This is in qualitative agreement with the results of Bechtold et al. (1994) and Dinshaw et al. (1994, 1995).

We also plot in Figure 19b the median velocity separation of the coincident lines as a function of Δr . The velocity of a line is defined as the center of the interval between the two points where $F = F_t$. Line pairs are identified using the same conditions as above (if there is more than one line satisfying these conditions, the one closest in velocity is chosen). Black squares show the median velocity separation of the chance coincident lines, obtained from random pairs of spectra as before. The median velocity differences are unobservably small for small separations (in agreement with the results of Smette et al. 1993), and they grow to $\sim 30 \text{ km s}^{-1}$ at $\Delta r = 100h^{-1}$ kpc.

Here again, we emphasize that measuring directly the cross-correlation function of the flux is also a powerful method of analysing the observations, in particular for comparison to these simulations. As we have already seen, our simulations do not predict correctly the number of high column density systems, which are effected by optical depth considerations not treated in this paper and which may be associated with dense regions in halos and are responsible for the large equivalent width lines. The weaker absorption lines tend to be blended, and their cross-correlation depends on how they are identified. Moreover, observations of the spectra of quasar pairs are often of relatively low signal-to-noise, so that only strong lines can be detected individually, but much information is present in the flux cross-correlation in regions of low absorption, which can be above the noise once it is averaged over a large region in the spectrum.

4.9. The HeII Gunn-Peterson Effect

The spectrum of a quasar below the rest-frame wavelength of the HeII Ly α line was recently observed for the first time. The first observation (Jakobsen et al. 1994) was consistent with no transmitted flux, and could put an upper limit of 0.2 to the fraction of transmitted flux. Later observations (Tytler et al. 1995; Davidsen et al. 1995) have found a fraction of transmitted flux closer to ~ 0.3 at $z = 3$.

Several calculations have been made of the expected HeII flux decrement from a population of clouds causing absorption lines with Voigt profiles, given certain fits to the observed distributions of column densities and b-parameters (Miralda-Escudé 1993; Jakobsen et al. 1994; Madau & Meiksin 1994). These calculations need to assume an extrapolation of the column density distribution to very low column densities, since the HeII decrement is dominated by the weakest lines which can cover most of the spectrum; furthermore, they all assume that the positions of the lines in the spectra are uncorrelated. In addition, there is an uncertainty in the relation of the HI and HeII b-parameters, depending on whether the velocity dispersion is of thermal or hydrodynamic origin.

The simulations of the gas causing the Ly α forest allow us to make a direct prediction of the HeII decrement, as a function of the ratio of the ionization rate of HI and HeII atoms, given by the spectrum of the photoionizing background, circumventing all of the above uncertainties. We assume that collisional ionization is negligible for both the neutral hydrogen and the HeII, and that the clouds are optically thin to a spatially uniform background of ionizing photons. In that case, the ratio of HeII to HI column densities is uniform through the intergalactic medium and all the clouds, and is given by $N_{\text{He II}} / N_{\text{HI}} = 1.7 (J_{\text{HI}} / J_{\text{He II}})$, and the ratio of the optical depths

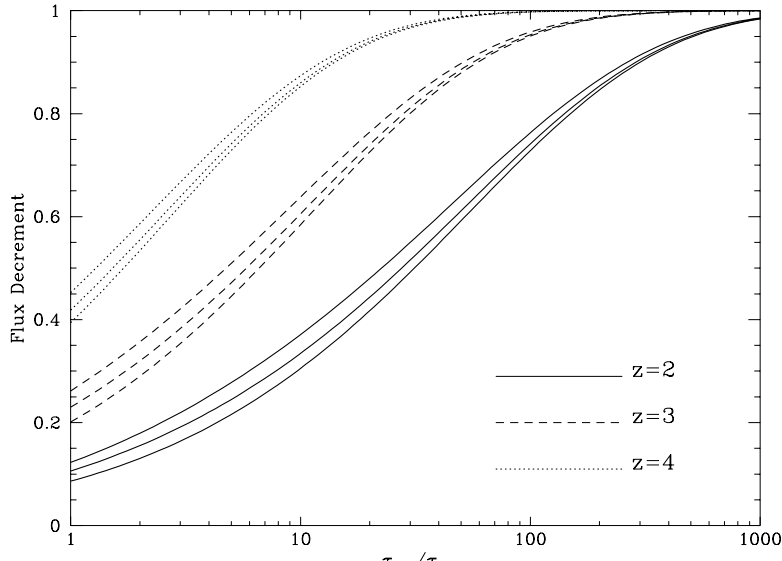


Fig. 20

Fig. 20: Average flux decrement as a function of a factor $\tau_{He\,II} / \tau_{HI}$ by which the optical depth of the spectra are multiplied. For each redshift, the upper line gives the flux decrement obtained from spectra without including thermal broadening, the upper line included thermal broadening for HI , and the middle line is for thermal broadening with half the velocity width, appropriate for $He\,II$. For fully ionized, optically thin clouds, and neglecting collisional ionization (which are good approximations for the low column density absorption lines dominating the contribution to the average flux decrement), the middle lines predict the $He\,II$ flux decrement in terms of the spectral shape of the ionizing background, where $\tau_{He\,II} / \tau_{HI} = 0.43 (J_{HI} / J_{He\,II})$.

given by any gas element at any position of the spectrum, without including thermal broadening, is $\tau_{HI} / \tau_{He\,II} = 0.43 (J_{HI} / J_{He\,II})$ (Miralda-Escudé 1993). The spectra then need to be convolved with thermal broadening with a width $b_{He\,II} = 0.5 b_{HI}$.

The predicted He II flux decrement from our L10 simulation is shown in Figure 20, as a function of the ratio $\tau_{He\,II} / \tau_{HI}$. At each redshift we plot three lines: the upper one is for spectra with the thermal broadening of HI (and therefore they are the same curves as in Fig. 10), the middle curve is for the thermal broadening of $He\,II$, and the lower curve is for no thermal broadening. Reducing the thermal broadening reduces the flux decrement, since more of the absorption is concentrated into saturated lines, and any gaps between the lines are left with less absorption. The small difference between the three curves denotes the importance of hydrodynamic motions, especially in the weak features of the spectrum. In particular, it implies that at the highest flux decrements the absorption is being produced by intergalactic gas in the voids, covering all the range of velocities in a spectrum (notice from §3, Figures 7, that the range of velocities within systems producing absorption lines is small).

If the observed flux decrement is 0.7 at $z = 3$, then we need $\tau_{He\,II} / \tau_{HI} \simeq 20$, which corresponds to $J_{HI} / J_{He\,II} \simeq 50$. From Figures 4a,b of Miralda-Escudé & Ostriker (1992), we

see that this ratio is slightly higher than what is predicted for a model of the ionizing background where the sources are quasars with a power-law spectrum $F_\nu \propto \nu^{-1.4}$, by about a factor of 2.5. The larger ratio of $J_{H\,I} / J_{He\,II}$ can easily be explained if the intrinsic spectrum of quasars is slightly softer between the ionization edges of HI and HeII or if hot stars (which have a soft spectrum) make a significant contribution. In fact, because of the effects of absorption by the Ly α clouds, the intrinsic spectrum of quasars needs to change by less than a factor 2.5 in the ratio $J_{H\,I} / J_{He\,II}$. This is still consistent with observations of the far UV and X-ray spectrum of quasars (Laor et al. 1994). The background of the spectrum produced in our simulation has too large a ratio $J_{H\,I} / J_{He\,II}$ (see Fig. 1), indicating that the chosen sources described in §2 were too soft and the reionization of HeII was not sufficiently advanced. In any case, a HeII flux decrement near 0.7 at $z = 3$ is entirely consistent with the HeII having been reionized by the expected sources of the ionizing background.

5. DISCUSSION

In §4, we have presented the predictions of the CDM+ Λ model we are examining for the Ly α forest, according to our simulations, and we have seen that they generally agree with the observed characteristics, although a much more precise and exact comparison with observations should be done in the future to establish quantitatively any differences of the observed spectra with the predicted ones by this and other theories. If it is indeed true that the gravitational collapse of structure from primordial fluctuations at high redshift is the origin of the Ly α forest, then we can derive several consequences for the average baryon density of the universe and the distribution of the baryons in the Ly α clouds. We analyze such implications in this Section.

5.1. Constraints on Ω_b

In §4.1, we have defined the quantity

$$\mu^2 \equiv (\Omega_b h^2)^2 / (h J_{H\,I}) , \quad (3)$$

which we have chosen to fit our predicted value of the average flux decrement in Ly α spectra to the observed one. We have then seen that this value leads to a correct prediction of the number of absorption lines near $N_{HI} = 10^{14} \text{ cm}^{-2}$, and gives a shape for the column density distribution that is similar to the observed one. We have also examined the dependence of our predicted average flux decrement and number of lines with the resolution and the size of the periodic box we use in the simulation, and have found that for fixed μ^2 , such effects can only be causing us to overestimate the average flux decrement and number of lines. Thus, in the model we assume in this paper the parameter μ^2 should probably not be lower than we have assumed because, as we see from Figure 10, the predicted flux decrement is already on the low side compared to observations, and it could only be made lower by the limitations in dynamic range of the simulation. There is still the possibility that a simulation evolved with a low value of $J_{H\,I}$ as needed to obtain the correct flux decrement would contain cooler gas that would lead to more absorption; unfortunately, we only have a simulation for a high value of $J_{H\,I}$, and we have had to assume that the only effect of lowering $J_{H\,I}$ is to increase the neutral fractions as $J_{H\,I}^{-1}$.

Determinations of the intensity of the ionizing background caused by quasars (which include the observationally known absorption by Ly α clouds) give values of $J_{HI} \simeq 0.3$ at the redshifts we are considering (e.g., Haardt & Madau 1995), and the value could be much larger owing to obscuration of quasars (see Fall & Pei 1995) and to the ionizing photons emitted by high-redshift galaxies. At the same time, observations of the proximity effect favor an intensity of the ionizing background of $J_{-21} \simeq 0.3 - 1$ (Bechtold 1994 and references therein). If we require $J_{-21} > 0.2$, then we need $\Omega_b > 0.05$ for $h = 0.65$, which is on the high side of the estimates from primordial nucleosynthesis constraints.

The parameter μ^2 cannot be obtained from the observations of the Ly α forest alone; the reason we can infer its value is that we use the predictions of our simulation for the nature of the clouds. We now ask what property of the absorbing systems is needed to infer μ^2 . Let us consider that the absorption systems over some column density range contain a fraction of the baryons Ω_c/Ω_b , and have a filling factor f of the volume in the universe. The gas density in the systems is then proportional to Ω_c/f , and the density of neutrals is proportional to $(\Omega_c/f)^2/J_{HI}$. The average distance between two absorbing systems along a line-of-sight, d , is observationally determined, and the pathlength through them is $d f$. Thus, the column density, which is also observed, is proportional to $(\Omega_c^2 d)/(J_{HI} f)$, so the quantity that is determined from observations alone is $\Omega_c^2/(J_{HI} f)$. To infer Ω_b^2/J_{HI} , we need both the volume filling factor and the fraction of baryons in the clouds. The reason why we infer a high value for μ^2 is that the filling factors in our theory are very large (essentially, the weakest lines are caused by a fluctuating Gunn-Peterson due to the intergalactic medium, which fills all the volume), even though the fraction of baryons contained in the clouds is very high, as we shall see below.

The high value of μ^2 that we require could be changed by the effects of faster cooling with a low J_{HI} mentioned above. Another possibility is that very thin slabs of cool gas are generically formed between shocks, and they are not resolved in our simulation. Thin slabs are always produced in one-dimensional calculations of pancake-collapse (e.g., Shapiro & Struck-Marcell 1985); the question is whether they could still be important (and provide a significant contribution to the neutral column densities) in three-dimensional systems with small-scale structure in the dark matter. Another possible effect is the presence of explosions, which could reduce the filling factor of the photoionized gas owing to the presence of hotter gas in the intergalactic medium. Basically, anything that can increase the density of the gas contributing most of the observed column density will reduce the required baryon content.

A similar line of reasoning has been employed by Rauch & Haehnelt (1995) to derive an upper limit to the thickness of the clouds given an upper limit to $\Omega_b h^2$ (using the reverse argument), and infer a large axis ratio given the observation of the line coincidences across the line of sight. The clouds in our simulations have thicknesses of the order of this upper limit; they certainly have relatively large axis ratios, since for column densities typical of the Ly α forest the absorbers originate in large-scale structures forming sheets and filaments.

5.2. The Fraction of Baryons in the Intergalactic Medium

There is no absolute distinction in our model between the intergalactic medium and the Ly α clouds. They both form a continuous gas density field in space over the whole universe. Thus,

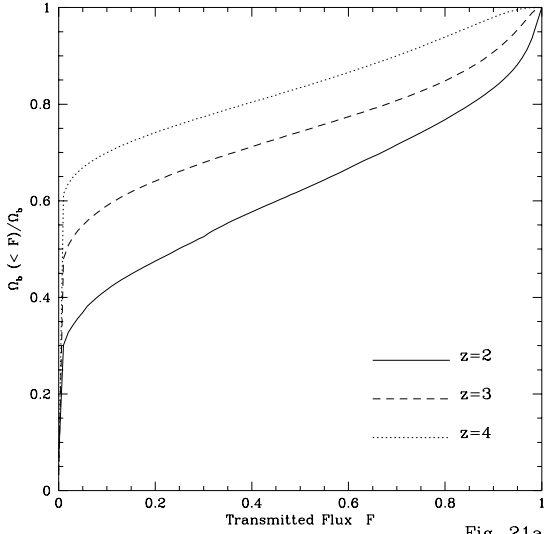


Fig. 21a

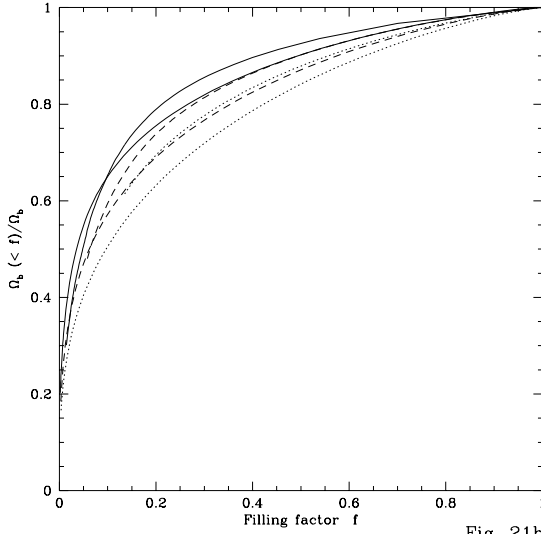


Fig. 21b

Fig. 21: (a) Fraction of baryons located at a velocity in the spectrum along random lines of sight where the transmitted flux is below F , in the L10 simulation. (b) Same curves as in (a), as a function of the filling factor in the spectra of regions below a fixed transmitted flux threshold (thick lines). The thin lines give the fraction of baryons in regions above a fixed density of neutral gas in real space, as a function of the volume-filling factor of these regions.

any separation of the intergalactic medium and the clouds necessarily involves some arbitrariness, depending on some parameter which can be varied. If we identify clouds as being the regions where the neutral hydrogen density in real space is above a certain threshold (as in §3), then we can identify the gas outside this region as the intergalactic medium. The cumulative distribution of the gas neutral density then gives the fraction of gas in the intergalactic medium at each isodensity contour. We do this in terms of the neutral density, since this is what is observed in the Ly α spectra; if contours of the total gas density were used, the results would not change too much, because the neutral fraction depends mostly on density, and the temperature tends to correlate well with density.

We can also identify clouds in the spectrum as in §4, defining a fixed optical depth as a threshold to separate absorption lines and the intergalactic medium. In this case, we can define the intergalactic medium as the gas having a hydrodynamic velocity along the line-of-sight which is not within a line (i.e., where the optical depth is above the threshold value). While this concept is less related to the physical properties of the gas (and, generally, any element of gas may be considered as part of the intergalactic medium or part of an absorption line depending on the line-of-sight that is chosen), it is more related to what can be observed in a spectrum. Shown in Figure 21a is the fraction of baryons outside absorption lines as a function of the threshold in transmitted flux, at three different redshifts (all quantities in this Section are for the L10 simulation and are obtained from the same 18000 rows described in §4.4, with the same value of μ^2 used throughout the paper; the same rows are used to calculate quantities from real space and from the spectra). In Figure 21b, the thick lines are the same quantity plotted in Figure 21a, but shown instead as a function of the filling factor in the Ly α spectra of regions with transmitted flux below different thresholds. The thin lines show the same fraction of baryons computed in real space, as explained above.

The evolution with redshift seen in Figure 21b is as expected: at lower redshift, structures have collapsed to a more evolved stage, with more baryons having moved into high density regions. Thus, the fraction of baryons in the intergalactic medium, defined to have any constant filling factor with redshift, decreases with time. However, we see from Figure 21a that the fraction of baryons which are in regions of the spectrum above a fixed transmitted flux is *increasing* remarkably fast with time. For example, taking a flux threshold $F_t = 0.5$, the fraction of baryons at velocities having less absorption is only 17% at $z = 2$, and it rises to 38% at $z = 4$. Of course, the filling factor for such regions at $z = 2$ is much larger than at $z = 4$ (see Fig. 11b); this is in fact the explanation why the gas appears to be “moving” to regions with less absorption. The gas actually moves, on average, to regions of higher overdensity, but this evolution is relatively slow and the more important effect is the expansion of the universe (and the gas structures that are forming), which causes the Gunn-Peterson optical depth to increase rapidly with redshift.

We also see from Figure 21b that the fraction of baryons in the Ly α spectra in regions of low absorption is lower than in real space. This is simply due to the faster expansion of the voids compared to the Hubble expansion. At low filling factors, the thick curves for the Ly α spectra drop below the ones for real space owing to the effects of thermal broadening and the velocity dispersion in collapsing systems. This figure shows clearly that when weak absorption features are detected in the Ly α spectra covering more than $\sim 50\%$ of the spectrum, then such absorption must be attributed to the fluctuating Gunn-Peterson effect from the intergalactic medium, since the gas causing this absorption occupies an even larger fraction of the real space volume. This must be true in any gravitational collapse theory for the Ly α clouds. Of course, in alternative theories of pressure-confined clouds the absorption lines could overlap over the whole Ly α spectrum while filling a small fraction of the volume of the universe, but such theories are in increasing conflict with observations of the transverse sizes of the clouds (Bechtold et al. 1994, Dinshaw et al. 1995).

Our conclusions then are that the weakest absorption features in the HI Ly α spectra (e.g., Hu et al. 1995), as well as the observed He II decrement (Jakobsen et al. 1994; Tytler et al. 1995; Davidsen et al. 1995), and the HI decrement in the highest redshift quasars (Schneider et al. 1991) are most likely to be our first detections of the intergalactic medium (since when the overall flux decrement is high, then the lines contributing to the decrement must have a large filling factor). These observations can still be interpreted alternatively in other theories where the clouds are pressure-confined and still fill a small fraction of the volume in real space when their absorption profiles overlap to fill most of the spectrum. However, such a model could not account for a correlation of the absorption fluctuations on large scales. If the absorption fluctuations between lines are found to be correlated on parallel lines of sight in a similar way as the strong lines [see Fig. 13(a,b)], irrefutable evidence will have been obtained for the detection of a photoionized intergalactic medium with density fluctuations originating, at least partially, in gravitational collapse.

5.3. The Fraction of Baryons in the Absorption Lines

We now address the fraction of baryons which is in absorption lines of different column densities in our simulation. All the baryons which are not in the intergalactic medium for any fixed flux threshold, as defined above, and have not been transformed into stars, have to be part of absorption lines. First, we show in Figure 22 the HI column density distribution at different filling factors. The thick lines are the same as shown in Figure 15a, and the thin lines is the column density distribution

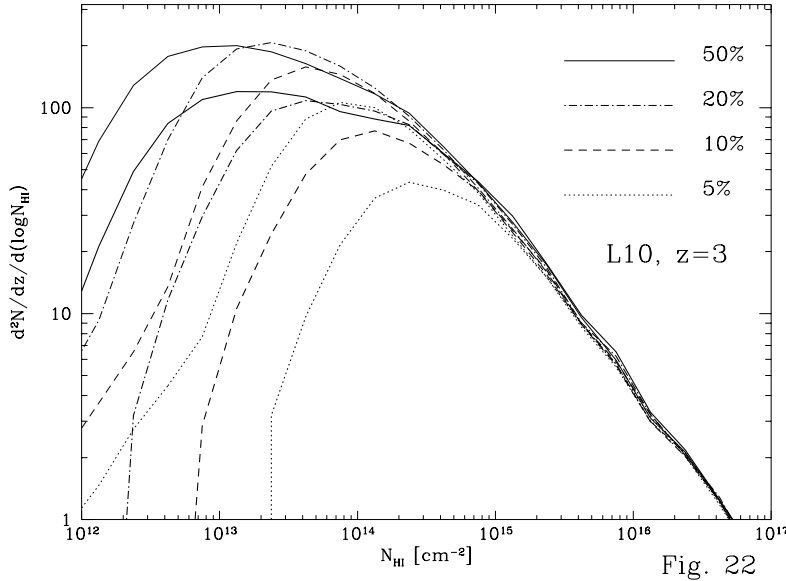


Fig. 22

Fig. 22: Column density distribution obtained from the spectra and from real space. Thick lines are the same as in Fig. 15a, thin lines are obtained from real space identifying clouds as intervals along a line of sight above a fixed neutral density, such that the volume-filling factor of these regions is the one specified in the figure.

obtained in real space, as in §3. The curves differ only at low column densities, with more weak lines being found in real space which are caused by small regions with the neutral gas density above the threshold; such regions tend to merge with bigger lines in the spectra, mostly due to the thermal broadening.

The cumulative fraction of baryons in absorption lines of different column density is shown in Figure 23a. Again, thick lines show the results obtained from the simulated spectra, whereas thin lines are for clouds defined in real space. We fix the filling factor of the “clouds” to 50% in both cases. The results are shown at three different redshifts, with the same line types as in Figure 21a. At the lowest column densities, the curves start at a value of Ω/Ω_b which indicates the fraction of baryons in the “intergalactic medium”, the 50% of the spectra (or real space) which is left outside the clouds. At the high end, the value of Ω/Ω_b does not reach unity because of the fraction of baryons that have turned into stars according to our algorithm (see §2), although there is also Poisson noise due to the small number of high column density systems found in the 18000 spectra we have used. In practice, this fraction of the baryons could also have been stabilized in rotating disks and be observed as a larger number of Lyman limit and damped absorption systems (see Katz et al. 1995), or could be in the form of molecular clouds in such galactic gaseous disks.

We also show in Figure 23b the same curves for the L3 and l3 simulations (*dash-dot and long dashed lines*), all at $z = 3$. More gas resides in low column density lines in the small box simulations, due to the absent large-scale power. However, the biggest difference is at high column densities: much of the gas in lines with $N_{HI} \sim 10^{16} \text{ cm}^{-2}$ in the L10 simulation has moved to higher column density

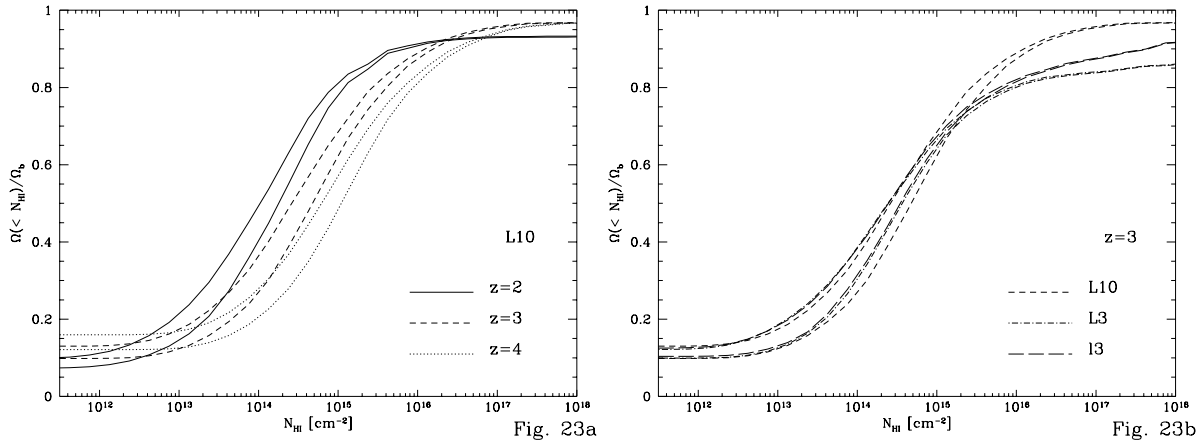


Fig. 23: Fraction of baryons contained in lines below a column density N_{HI} , for clouds identified in real space (thin lines) and in the spectra (thick lines), using in both cases a filling factor of 50%. At low column densities, the curves approach the fraction of baryons which are left in the remaining 50% of the volume in real space, or in the spectra, while at high column densities the difference of Ω/Ω_b from unity is the fraction of baryons turned into stars (however, there is also a Poisson error due to the limited number of high column density systems in the set of 18000 spectra used to do the calculation).

systems or been turned into stars in the L3 and l3 simulations. This should be related to the higher resolution of the small box simulations (notice the difference between L3 and l3), although the large-scale power could also be important: it may be more difficult for the gas to move from filamentary structures to the higher density halos when it continues to be shocked as the filaments merge with each other (a process which has almost stopped in the small box simulations by $z = 3$).

In our model, *about 80% to 90% of the baryons in the universe are in the Ly α clouds*, with practically no change from $z = 4$ to $z = 2$. The majority of them are in clouds with column densities over the range 10^{14} to $10^{15.5} \text{ cm}^{-2}$. The typical column densities decrease by a factor ~ 5 from $z = 4$ to $z = 2$, as a consequence of the expansion of the clouds and the progressive heating of the gas as larger scale structures collapse. The higher temperatures (see Fig. 9b) reduce the recombination coefficient and increase collisional ionization, decreasing therefore the neutral column densities.

This result, that most of the baryonic mass in the universe is in features giving column densities of $N_{HI} = 10^{14} - 10^{15} \text{ cm}^{-2}$ is in apparent contrast to the well known result that most of the *neutral* gas is observed to be in very high column density systems (the damped Lyman alpha systems associated with proto galaxies) having $N_{HI} > 10^{20} \text{ cm}^{-2}$. The reason is simply the high state of ionization of most of the gas in the low column density systems and the increasing neutral fraction as a function of column density shown in Figure 9a.

5.4. Origin of the Column Density Distribution

Having seen the fraction of baryons in clouds of different column density, we shall now give an interpretation of the form of the column density distribution we have found from the simulation. As

we see from Figure 22, the column density distribution in real space is very close to the one obtained from the simulated spectra.

The neutral column density of a region of overdensity δ and length L is proportional to $\delta^2 LT^{-0.7}$, where T is the gas temperature and is included to reflect the variation of the recombination coefficient. If Ω_c/Ω_b is the fraction of baryons in such “clouds”, then their filling factor should be $f = (\Omega_c/\Omega_b) \delta^{-1}$, and the number of clouds found per unit length along a line of sight is

$$dN/d\log N_{HI} = f/L = \frac{\Omega_c}{\Omega_b} (\delta L)^{-1} \propto (\Omega_c/\Omega_b) (N_{HI} LT^{0.7})^{-1/2}. \quad (4)$$

Let us apply this to some special cases. In the case of an isothermal halo, where the gas density varies as L^{-2} and the neutral column density as L^{-3} , and $\Omega_c(N_{HI})/\Omega_b \propto L \propto N_{HI}^{-1/3}$, we obtain the well-known result that $dN/d\log N_{HI} \propto N_{HI}^{-2/3}$ (e.g., Rees 1988); in general, for spherical halos with the gas density $\rho \propto L^{-\alpha}$, we have $dN/d\log N_{HI} \propto N_{HI}^{2/(1-2\alpha)}$.

At column densities where the typical structures are filamentary in nature, the scales across the systems, L , are approximately independent of the column density across them. The filaments have column densities up to $N_{HI} \sim 10^{15} \text{ cm}^{-2}$, and we see from Fig. 23a that the baryon content is approximately constant in the range 10^{14} cm^{-2} to 10^{15} cm^{-2} . We then expect $dN/d\log N_{HI} \propto N_{HI}^{-0.5}$, as is indeed found. The pathlength L starts decreasing at higher column densities, when the systems have a more spheroidal geometry. In addition, at column densities above 10^{15} cm^{-2} , the fraction of baryons in clouds per unit $\log N_{HI}$ starts declining, and the temperatures increase (Fig. 9c). All these effects result in the steepening of the column density distribution above 10^{15} cm^{-2} . At low column densities the distribution becomes shallower, due to the small baryon content of low-column density sheets. Although a large number of weak lines are inferred when deblending methods are used, most of these lines are in fact not real systems but are only needed to fit the outer profiles of stronger lines.

5.5. Relation to Galaxy Formation

The densest regions (overdensity ≥ 100) of the inter-connecting network of baryonic matter distribution are cooling and collapsing, with velocity dispersions typical of dwarf galaxies at present ($v \sim 50 - 100 \text{ km s}^{-1}$). The gas in these regions may either start forming stars, or form relatively stable gaseous disks in the more massive regions that could be responsible for the damped absorption systems, and could later merge to form present-day galaxies (see Katz et al. 1995).

It is unavoidable that, during the galaxy formation process, absorption systems should be produced. Present galaxies are surrounded by dark matter halos, and in order for the baryons to have separated out and accumulated in the central luminous parts, gas must have dissipated and flown in through the halos at some point in the past. During this process, gas is shock-heated to the galactic virial temperatures, and when radiative cooling is effective in free-falling gas temperature perturbations are amplified (Field 1965) and one will naturally form pressure-confined, photoionized clouds embedded in hotter gas (e.g., Fall & Rees 1985). Such clouds may be responsible for some of the high column density systems that we do not reproduce in our simulation. In addition, our treatment of the ionizing radiation does not allow proper radiative transfer (rather, we assume that the radiation field is uniform across the simulation box), so we must have underestimated column

densities of systems whose optical depths approach unity ($N_{HI} \sim 10^{17}$). These two effects can probably explain the observed number of Lyman limit systems, and they might also contribute significantly to the observed damped Ly α systems.

Regardless of whatever uncertainties might exist in the simulations, what is clear from the results of this paper is that the history of galaxy formation is closely related to the Ly α absorption systems. Any gas which has not been incorporated into galaxies at high redshift should be in the Ly α clouds, and different theories on the rate at which gas can cool and form galaxies would lead to different predictions on the number of lines of different column densities. The agreement of our simulation with the observed absorption lines at the column densities where most of the baryonic material is contained suggests that, indeed, most of the baryons had not collapsed into galaxies at $z \sim 3$. In fact, if more baryons had collapsed in very dense regions the problem of accounting for the number of Ly α forest lines given the lower limits on J_{HI} would be made much more severe.

In several studies of galaxy formation, it was found that small galaxies at high redshift accreted a large fraction of the gas, implying that present galaxies could only have formed from mergers of a large number of small galaxies (see White & Frenk 1991; Kauffmann, White, & Guiderdoni 1993; Lacey et al. 1993). This has been referred to as the “overcooling problem”. Part of the problem may be related to the use of simple Press-Schechter models, where it is assumed that much of the gas collapses into dense clumps after the first generation of objects where the gas can collapse is formed. This is not borne out by our simulations, which imply a slow depletion of the gas from the intergalactic medium (see Fig. 21b), and suggest a picture where much of the gas stays in filamentary structures which merge with each other to form larger-scale filaments before much of the gas has a chance to collapse to very dense clumps.

A solution that has been investigated is the effect of photoionization on slowing or reversing the cooling rate and hence stabilizing the collapse on small scales (Efstathiou 1992; Quinn, Katz, & Efstathiou 1995; Steinmetz 1995). In all the simulations we have performed for a variety of models (see Ostriker & Cen 1995 and references therein), we find that only a small fraction (2-10%) of all the baryons has collapsed into compact objects (stars/galaxies) at present. In fact, we found that most of the gas resides in two major components with comparable masses: “Void” and “Hot IGM”. The former corresponds to the Ly α clouds that we are finding here but the latter (with temperatures in the range $10^5 - 10^7$ K and intermediate densities) is a totally separate and new component. This may be affected by the relatively poor resolution of our previous simulations, but our new simulations with higher resolution, including those presented in this paper, yield results in terms of collapsed fraction consistent with our previous findings.

We suspect that the current popular variants of the CDM model will yield the collapsed baryonic fraction consistent with observations, while HDM-like models and PBI-like models will perhaps produce too small and too large a fraction of collapsed baryons, respectively. But higher resolution simulations of these models with proper handling of the radiative processes are the only means to give us a definitive answer.

6. CONCLUSIONS

The model we have investigated here is one of several variants of the basic Cold Dark Matter

scenario spawned after the COBE observations showed that the simplest CDM model, while close in many respects to reality, could not be correct in detail (cf. Efstathiou 1991, Ostriker 1993). This particular variant is not unique in its ability to fit all known observational constraints (cf. Ostriker & Steinhardt 1995), but, we stress it was adopted for reasons having nothing to do with observations of the Lyman alpha forest. Bond et al. (1988) argued at a very early time, on the basis of quite general considerations, that this type of model should produce absorption line features roughly like those observed in the Lyman alpha forest, and we find that contention to be correct.

In massive and detailed simulations of the evolution of a CDM+ Λ model we find that the normal physics of self-gravitating fluids containing dark matter, baryons with a primeval composition and ionizing radiation will generate an interlocking structure of “sheets”, “filaments” and “clumps” surrounding “voids” of growing size. Once the gas is photoionized and photoheated, the thermal energy (as symbolized by the Jeans length and Jeans mass) smoothes out fluctuations on small scales in the gaseous component (but not of course in the dark matter component).

The weak shocks induced by the flows in gas are regions of moderate overdensity $10^{0.5} - 10^{1.5}$ which correspond to overdensities in neutral hydrogen of $10^{1.0} - 10^{3.0}$ and column densities of $10^{14} - 10^{15}$. Such systems contain most of the baryons at redshifts $z = 4$ to $z = 2$. The somewhat smaller fraction of gas in the voids produces a fluctuating Gunn-Peterson effect.

Gas drains along the filaments, accumulating in higher density systems (where presumably galaxies form). The relatively small fraction of the gas ($\sim 10\%$) associated with these systems is not computed accurately by our simulations due to a lack of resolution at high density (as well as other physical effects we do not include, such as self-shielding). Consequently, we do not expect our predictions for absorbers with $N_{HI} \gtrsim 10^{16} \text{ cm}^{-2}$ to be accurate, and indeed the number of them obtained in the simulations is significantly lower than observed. But, for the bulk of the gas in the voids and in the low and moderate column density systems, our numerical methods are probably accurate enough to fairly predict what our adopted model would imply.

First we must adjust the parameter $\mu \equiv \Omega h^2 / (J_{HI} h)^{1/2}$ to match observations. This is the only parameter we have adjusted on a *post hoc* fashion. If we take $\Omega_b h^2$ to be the value given by standard nucleosynthesis arguments ($\Omega h^2 = 0.0125 \pm 0.0025$; Walker et al. 1991), then we require $J_{-21} h = 0.1 \times 0.65 = 0.065$. As we have discussed, this is too low compared to the lower limit of J_{-21} obtained from the abundances of the observed quasars, indicating that our model requires a slightly larger Ω_b than the upper limit from primordial nucleosynthesis.

With the parameter μ adjusted as described, we find that there is an excellent agreement between the computations and the observations. The typical feature that produces a Lyman alpha cloud is gas that collapsed to form mini-pancakes and filaments with collapse velocities of several tens of km/s. It is observed in its post-shock phase having an overdensity of $\sim 10^1$, a neutral fraction of $\sim 10^{-5}$, a Doppler b parameter of $\sim 25 \text{ km/s}$ (produced by a similar contribution of hydrodynamic motions and thermal broadening) and an extent along the line of sight of $\sim 100 \text{ kpc}$. The gas is typically expanding close to the Hubble rate for systems with $N_{HI} \lesssim 10^{15} \text{ cm}^{-2}$. Neutral fraction increases from $10^{-5.3}$ at $N_{HI} = 10^{13} \text{ cm}^{-2}$ to $10^{-4.0}$ to at $N_{HI} = 10^{16.0} \text{ cm}^{-2}$, with the characteristic gas temperature increasing from $10^{4.3}$ to 10^5 in that same range of column densities. The temperatures increase with time as shocks from longer waves produce higher velocities.

We find approximately the correct redshift dependence of Lyman alpha forest and attribute

it very simply to the same redshift dependence of the classical Gunn-Peterson effect. Roughly speaking, each feature in the low column density Ly α forest preserves its characteristics, but its opacity changes by approximately $(1+z)^{9/2}$, as expected for comoving, photoionized gas in a nearly constant radiation field.

The correlations in spectral features both along and perpendicular to the line of sight are consistent with observations, with detailed predictions testable only when simulations and real data are analyzed in the same way. The distribution of equivalent widths is also as observed, with the same caveats as mentioned above. We do predict a broad distribution of b values and a weak correlation of b with N_{HI} , which should allow a detailed check of the overall scenario. The ratio of the He II to HI flux decrements at different redshifts is predicted in terms of the spectral shape of the background, and we find that a model where quasars are the emitting sources is consistent, although softer sources making a contribution to the background similar to quasars are also possible.

These results, and the fact that other models of structure formation by hierarchical clustering (HKWM and Zhang et al. 1995) give results that are similar to ours suggest that the value required for the parameter μ could provide a reliable measurement. The main reason why we obtain a very large baryon content in the Ly α forest, even when choosing the lowest reasonable value for J_{-21} , is the large volume-filling factor of the clouds implied by our models. The only way to decrease our estimate of Ω_b^2/J_{HI} from the Ly α forest observations is to reduce the volume-filling factor (or increase the cloud overdensities). This could be the case if gas was able to cool to lower temperatures and contract to higher densities than in our simulation, forming thin slabs in the center of the filamentary and sheet-like structures which we might not resolve. This will be investigated in more detail in Gnedin et al. (1995). If such thin slabs were important, they would probably produce narrow components in the line profiles and, at the same time, any tendency to fragmentation on small scales should cause small-scale differences in the line profiles on parallel lines of sight. In fact, it seems difficult for this interpretation that clouds with high densities could be correlated over large transverse scales, as implied by the observations of Bechtold et al. and Dinshaw et al. , and practically not change their line profiles on scales of a few kpc (Smette et al. 1992). Further observations of the degree of similarity of the absorption profiles in lensed quasars are essential to make a strong case for the large baryon content of the clouds.

A value of Ω_b as large as required by our models would be consistent with a baryon fraction $\sim 15\%$ in clusters (e.g., White & Fabian 1995) for the values of our adopted model $\Omega = 0.4$ and $h = 0.65$. This would then exacerbate the problem of the missing baryons at the present time. One possibility is that a large fraction of baryons are still in the intergalactic medium, forming a present-time “Ly α forest” on much larger scales and much higher temperatures ($T \sim 10^5 - 10^6$ K) than at high redshift. This would yield very weak neutral hydrogen absorption lines owing to the high degree of collisional ionization. Only the low temperature tail of the gas would be seen in the low-redshift Ly α spectra. Given the small density of baryons observed in galaxies and the X-ray emitting gas ($\Omega_b \simeq 0.003$; Persic & Salucci 1992), a very large (perhaps implausible) fraction of the baryons would have to be in such low-density structures. The missing baryons might also have formed low-mass stars in galaxy halos (e.g., Fabian, Nulsen, & Canizares 1991), might be in low surface brightness, undetected galaxies (e.g., McGaugh 1994), or might reside in low surface brightness stellar halos around normal galaxies and in clusters of galaxies (Sackett et al. 1994).

We thank John Bahcall, Mike Fall, Piero Madau, Martin Rees, and David Weinberg for stimulating discussions, and Bob Carswell, John Webb, and Andrew Cooke for providing us with the latest version of their profile fitting software and very helpful discussions and advice on its usage. The simulation was performed on Convex-3880 in NCSA with time allocation provided by M. Norman. RC and JPO are supported by NASA grant NAGW-2448 and and NSF grants AST91-08103 and ASC-9318185; JM gratefully acknowledges support from the W. M. Keck Foundation, and from NASA grant NAG-51618. MR is supported by NASA through grant HF-01075.01-94A from the Space Telescope Science Institute, which is operated by the Association of Universities for Research in Astronomy, Inc., under NASA contract NAS5-26555.

Finally, we would like to add a note on the availability of the simulations presented in this paper to the larger cosmological/astrophysical community. We are making the synthetic spectra generated from these simulations available freely to users in the community. The simulated quasar spectra can be found on the Web page "<http://astro.princeton.edu/cen/LYA/entry.html>".

REFERENCES

Arons, J., 1972, *ApJ*, 172, 553
Arons, J., & Wingert, D. W. 1972, *ApJ*, 177, 1
Bahcall, J. N., & Spitzer, L. 1969, *ApJ*, 156, L63
Bechtold, J. 1994, *ApJS*, 91, 1
Bechtold, J., Crots, A. P. S., Duncan, R. C., & Fang, Y. 1994, *ApJ*, 437, L83
Bi, G. 1993, *ApJ*, 405, 479
Bond, J. R., Szalay, A. S., & Silk, J., 1988, *ApJ*, 324, 627
Carswell, R. F., Lanzetta, K. M., Parnell, H. C., & Webb, J. K., 1991, *ApJ*, 371, 36
Cen, R. 1992, *ApJS*, 78, 341
Cen, R., Gnedin, N.Y., & Ostriker, J.P, 1993, *ApJ*, 417, 387
Cen, R., Miralda-Escudé, J., Ostriker, J. P., & Rauch, M. 1994, *ApJ*, 437, L9(**Paper I**)
Cen, R., & Ostriker, J. P, 1992, *ApJ*, 399, L113
——— 1993a, *ApJ*, 404, 415
——— 1993b, *ApJ*, 417, 415
Charlton, J. C., Salpeter, E. E., & Hogan, C. J. 1993, *ApJ*, 402, 493
Cristiani, S., D'Odorico, S., Fontana, A., Giallongo, E., & Savaglio, S. 1995, *MNRAS*, 273, 1016
Davidson, A., et al. 1995, preprint
Dinshaw, N., Impey, C. D., Foltz, C. B., Weymann, R. J., & Chaffee, F. H. 1994, *ApJ*, 437, L87
Dinshaw, N., Foltz, C. B., Impey, C. D., Weymann, R. J., & Morris, S. L. 1995, *Nature*, 373, 223
Edelson, & Malkan 1986, *ApJ*, 308, 59
Efstatouli, G. 1991, *Physica Scripta*, T36, 88
——— 1992, *MNRAS*, 256, 43p
Efstatouli, G., Bond, J. R., & White, S. D. M. 1992, *MNRAS*, 258, 1p
Fabian, A. C., Nulsen, P. E. J., & Canizares, C. R. 1991, *A&A Rev.*, 2, 191
Fall, S. M., & Pei, 1993, *ApJ*, 402, 479
——— 1995, in *QSO Absorption Lines*, Proc. ESO Workshop, ed. G. Meylan (Heidelberg: Springer), p. 23
Fall, S. M., & Rees, M. J. 1985, *ApJ*, 298, 18
Fardal, M. A., & Shull, J. M. 1993, *ApJ*, 415, 524
Field, G. 1965, *ApJ*, 142, 153
Fransson, C., & Epstein, R. 1982, *MNRAS*, 198, 1127
Gnedin, N., et al. 1995, in preparation
Gunn, J. E., & Peterson, B. A. 1965, *ApJ*, 142, 1633
Haardt, F., & Madau, P. 1995, submitted to *ApJ* (astro-ph 9509093)
Harten, 1984, *J. Comp. Phys.*, 49, 357
Hernquist, L., Katz, N., Weinberg, D. H., & Miralda-Escudé, J. 1995, *ApJ* Let, submitted (**HKWM**)
Hu, E. M., Kim, T.-S., Cowie, L. L., Songaila, A., & Rauch, M. 1995, *AJ*, 110, 1526
Ikeuchi, S. 1986, *Astrop. Space Sci.*, 118, 509
Ikeuchi, S., & Ostriker, J. P. 1986, *ApJ*, 301, 522
Jakobsen, P., Boksenberg, A., Deharveng, J. M., Greenfield, P., Jedrzejewski, R., & Paresce, F. 1994, *Nature*, 370, 35
Jenkins, E. B., & Ostriker, J. P. 1991, *ApJ*, 376, 33

Katz, N., Weinberg, D. H., Hernquist, L., & Miralda-Escudé, J. 1995, ApJLet, submitted
Kauffmann, G., White, S. D. M., & Guiderdoni, B. 1993, MNRAS, 264, 201
Kofman, L., Gnedin, N., & Bahcall, N. 1993, ApJ, 413, 1
Lacey, C. G., Guiderdoni, B., Rocca-Volmerange, B., & Silk, J. 1993, MNRAS, 402, 15
Laor, A., Fiore, F., Elvis, M., Wilkes, B. J., & McDowell, J. C. 1994, ApJ, 435, 611
Lu, L., Wolfe, A. M., & Turnshek, D. A. 1991, ApJ, 367, 19
Madau, P., & Meiksin, A. 1994, ApJ, 433, L53
McGaugh, S. S. 1994, ApJ, 462, 135
Miralda-Escudé, J., & Ostriker, J. P. 1992, ApJ, 392, 15
Miralda-Escudé, J. 1993, MNRAS, 262, 273
Miralda-Escudé, J., & Rees, M. J. 1993, MNRAS, 260, 624
——— 1994, MNRAS, 266, 343
Morris, S. L., & van den Bergh, S. 1994, ApJ, 427, 696
Murdoch, H. S., Hunstead, R. W., Pettini, M., & Blades, J. C. 1986, ApJ, 309, 19
Ostriker, J. P. 1993, ARA&A, 31, 689
Ostriker, J. P., & Cen, R. 1995, submitted to ApJ
Ostriker, J. P., & Ikeuchi, S. 1983, ApJ, 268, L63
Ostriker, J. P., & Steinhardt, P. 1995, Nature, in press
Peebles, P. J. E. 1980, *The Large-Scale Structure of the Universe* (Princeton Univ. Press: Princeton)
Petitjean, P., Mückel, J. P., & Kates, R. E., 1995, A&A, 295, L9
Petitjean, P., Webb, J. K., Rauch, M., Carswell, R. F., & Lanzetta, K., 1993, MNRAS, 262, 499
Persic, M., & Salucci, P. 1992, MNRAS, 258, 14p
Press, W. H., & Rybicki, G. B. 1993, ApJ, 418, 585
Press, W. H., Rybicki, G. B., & Schneider, D. P. 1993, ApJ, 414, 64
Quinn, T., Katz, N., & Efstathiou, G. 1995, preprint
Rauch, M., Carswell, R. F., Chaffee, F. H., Foltz, C. B., Webb, J. K., Weymann, R. J., Bechtold, J., & Green, R. F. 1992, ApJ, 390, 387
Rauch, M., & Haehnelt, M. G. 1995, MNRAS, 275, L76
Rauch, M., et al. 1995, in preparation
Rees, M. J. 1986, MNRAS, 218, 25p
——— 1988. In: *QSO Absorption Lines*, p. 107, ed. J. C. Blades et al. , Cambridge Univ. Press, Cambridge.
Reisenegger, A., & Miralda-Escudé, J. 1995, ApJ, 449, 476
Ryu, D., Ostriker, J. P., Kang, H., & Cen, R. Y. 1993, ApJ, 414, 1
Sackett, P. D., Morrison, H. L., Harding, P., & Boroson, T. A. 1994, Nature, 370, 441
Sargent, W. L. W., Steidel, C. C., & Boksenberg, A. 1989, ApJS, 69, 703
Sargent, W. L. W., Young, P. J., Boksenberg, A., & Tytler, D. 1980, ApJS, 42, 41
Scalo, J.M. 1986, Fund. Comis Phys., 11, 1
Schneider, D. P., Schmidt, M., & Gunn, J. E. 1991, AJ, 101, 2004
Schneider, D. P., et al. 1993, ApJS, 87, 45
Shapiro, P., & Struck-Marcel, P. 1985, ApJS, 57, 205
Smette, A., Surdej, J., Shaver, P. A., Foltz, C. B., Chaffee, F. H., Weymann, R. J., Williams, R. E., & Magain, P. 1992, ApJ, 389, 39
Smette, A., Surdej, J., Shaver, P. A., Reimers, D., Wisotzki, L., & Köhler, T. 1995, A&A, in press

Steinmetz, M. 1995, preprint

Stengler-Larrea, E., et al. 1995, ApJ, 444, 64

Stompor, R., & Gorski, K. M. 1994, ApJ, 422, L41

Storrie-Lombardi, L., et al. 1994, ApJ, 427, L13

Sunyaev, R. A., & Zel'dovich, Ya. B. 1972, A&A, 20, 189

Tytler, D., Fan, X.-M., Burles, S., Cottrell, L., Davis, C., Kirkman, D., & Zuo, L. 1995, in *QSO Absorption Lines*, Proc. ESO Workshop, ed. G. Meylan (Heidelberg: Springer), p. 289

Walker, T. P., Steigman, G., Schramm, D. N., Olive, K. A., & Kang, H. S. 1991, ApJ, 376, 51

Wang, B. 1993, ApJ, 415, 174

——— 1995, ApJ, 444, L17

Webb, J. K., Barcons, X., Carswell, R. F., & Parnell, H. C. 1992, MNRAS, 255, 319

White, M., & Bunn, E 1995, preprint

White, D., & Fabian, A. C. 1995, MNRAS, 273, 72

White, S. D. M., & Frenk, C. S. 1991, ApJ, 379, 25

Williger, G. M., Baldwin, J. A., Carswell, R. F., Cooke, A. J., Hazard, C., Irwin, M. J., McMahon, R. G., & Storrie-Lombardi, L. J. 1994, ApJ, 428, 574

Zhang, Y., Anninos, & Norman, M. 1995, submitted to ApJ

Zuo, L. 1992a, MNRAS, 258, 36

——— 1992b, MNRAS, 258, 45

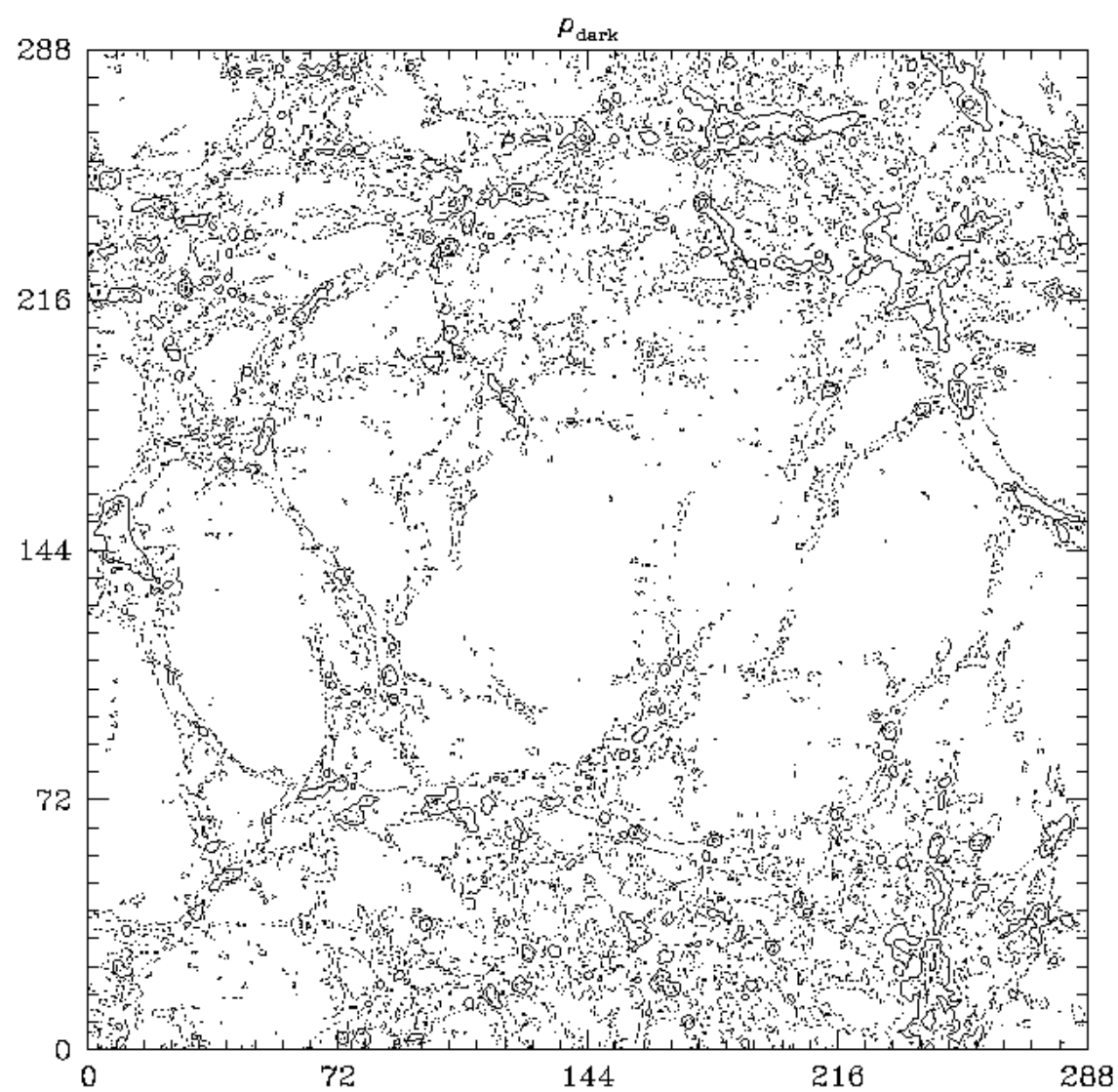


Figure 2b

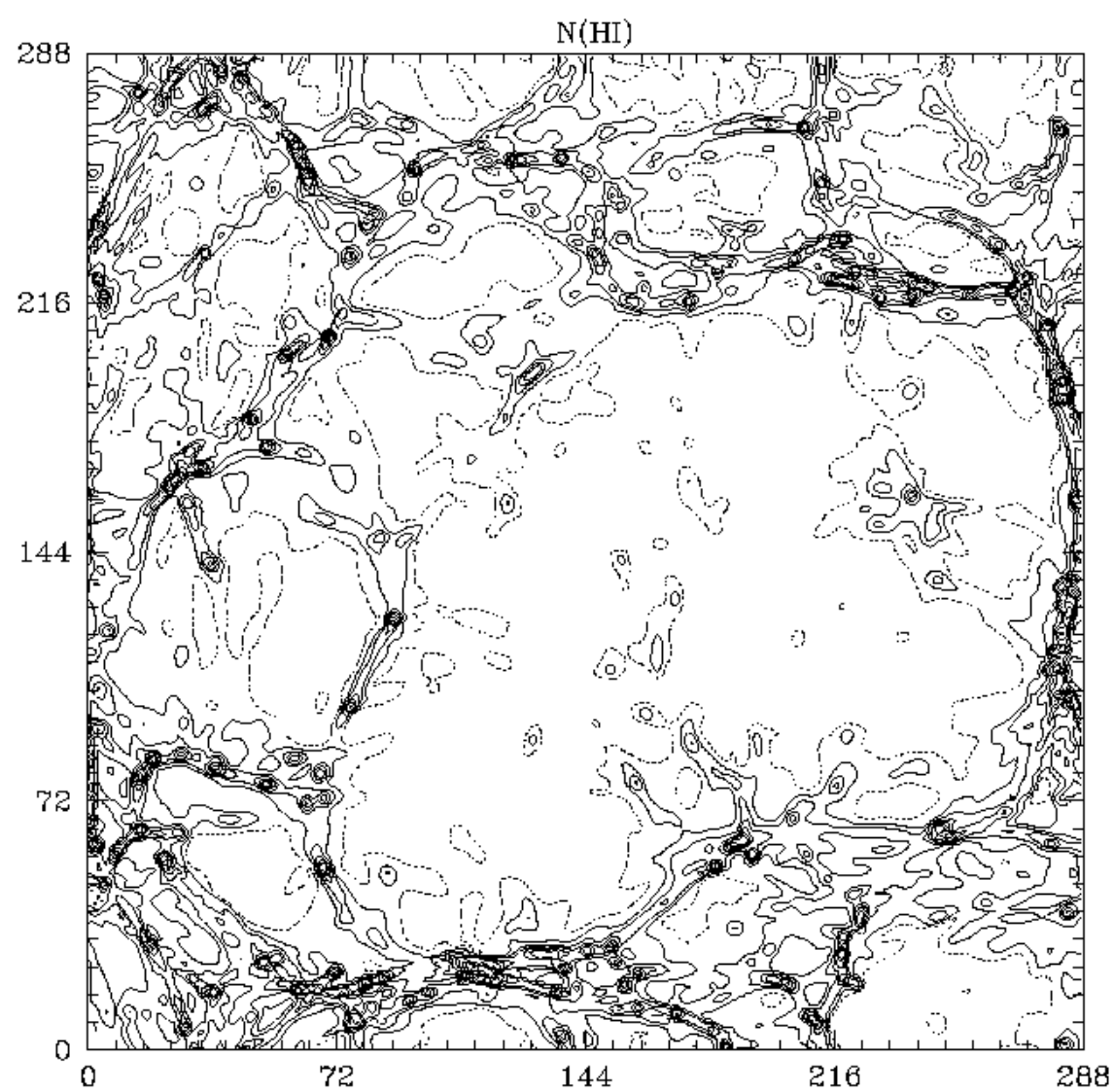


Figure 2c

